

REPORT DOCUMENTATION PAGE			Form Approved OMB NO. 0704-0188		
<p>The public reporting burden for this collection of information is estimated to average 1 hour per response, including the time for reviewing instructions, searching existing data sources, gathering and maintaining the data needed, and completing and reviewing the collection of information. Send comments regarding this burden estimate or any other aspect of this collection of information, including suggestions for reducing this burden, to Washington Headquarters Services, Directorate for Information Operations and Reports, 1215 Jefferson Davis Highway, Suite 1204, Arlington VA, 22202-4302. Respondents should be aware that notwithstanding any other provision of law, no person shall be subject to any penalty for failing to comply with a collection of information if it does not display a currently valid OMB control number.</p> <p>PLEASE DO NOT RETURN YOUR FORM TO THE ABOVE ADDRESS.</p>					
1. REPORT DATE (DD-MM-YYYY) 07-12-2013		2. REPORT TYPE Final Report		3. DATES COVERED (From - To) 25-Aug-2008 - 24-Aug-2013	
4. TITLE AND SUBTITLE Final Report: Metal-Semiconductor Nanocomposites for High Efficiency Thermoelectric Power Generation			5a. CONTRACT NUMBER W911NF-08-1-0347		
			5b. GRANT NUMBER		
			5c. PROGRAM ELEMENT NUMBER 7620AM		
6. AUTHORS Ali Shakouri, Nobby Kobayashi, Zhixi Bian, John Bowers, Art Gossard, Arun Majumdar, Rajeev Ram, Tim Sands, Josh Zide, Lon Bell			5d. PROJECT NUMBER		
			5e. TASK NUMBER		
			5f. WORK UNIT NUMBER		
7. PERFORMING ORGANIZATION NAMES AND ADDRESSES University of California - Santa Cruz Office of Sponsored Projects The Regents of the University of California, Santa Cruz Santa Cruz, CA 95064 -1077			8. PERFORMING ORGANIZATION REPORT NUMBER		
9. SPONSORING/MONITORING AGENCY NAME(S) AND ADDRESS (ES) U.S. Army Research Office P.O. Box 12211 Research Triangle Park, NC 27709-2211			10. SPONSOR/MONITOR'S ACRONYM(S) ARO		
			11. SPONSOR/MONITOR'S REPORT NUMBER(S) 54530-MS-DRP.30		
12. DISTRIBUTION AVAILABILITY STATEMENT Approved for Public Release; Distribution Unlimited					
13. SUPPLEMENTARY NOTES The views, opinions and/or findings contained in this report are those of the author(s) and should not be construed as an official Department of the Army position, policy or decision, unless so designated by other documentation.					
14. ABSTRACT Demonstrated high ZT~1.7 at 800K for the first time in nanostructured III-V material (0.12-0.5% ErAs:InGaAs). Successful electron transport modeling can explain temperature dependent Seebeck coefficient and mobility without fitting parameters. For the case of 0.8% TbAs:InGaAs, a ZT of 1.04 at 600K was demonstrated. Interestingly power factor enhancement for TbAs is much bigger than that for ErAs nanoparticles. However ErAs nanoparticles give higher thermal conductivity due to their smaller size (1nm vs. 2-5nm). Detailed experimental optimization of a ErSb-InGaAs/InSb lead to ZT=0.57 at 520K. In the case of metal/semiconductor multilayers					
15. SUBJECT TERMS thermoelectric, thermionic, Seebeck, transport					
16. SECURITY CLASSIFICATION OF:			17. LIMITATION OF ABSTRACT UU	15. NUMBER OF PAGES	19a. NAME OF RESPONSIBLE PERSON Ali Shakouri
a. REPORT UU	b. ABSTRACT UU	c. THIS PAGE UU			19b. TELEPHONE NUMBER 765-496-6105

Report Title

Final Report: Metal-Semiconductor Nanocomposites for High Efficiency Thermoelectric Power Generation

ABSTRACT

Demonstrated high $ZT \sim 1.7$ at 800K for the first time in nanostructured III-V material (0.12-0.5% ErAs:InGaAs). Successful electron transport modeling can explain temperature dependent Seebeck coefficient and mobility without fitting parameters. For the case of 0.8% TbAs:InGaAs, a ZT of 1.04 at 600K was demonstrated. Interestingly power factor enhancement for TbAs is much bigger than that for ErAs nanoparticles. However ErAs nanoparticles give higher thermal conductivity due to their smaller size (1nm vs. 2-5nm). Detailed experimental optimization of p-ErSb:In_xGa_{1-x}Sb lead to $ZT=0.57$ at 530K. In the case of metal/semiconductor multilayers, observed giant cross-plane Seebeck coefficients of 2,560 μ V/K at room temperature and 16,640 μ V/K at 360 K, and extremely low room temperature thermal conductivity of 0.92 W/mK for La_{0.67}Sr_{0.33}MgO₃/LaMnO₃ perovskite oxide metal/semiconductor superlattices. Excellent agreement with the first principle calculations. First measurements of Seebeck for nitride superlattice (130 μ V/K at 700K). Matches theoretical Seebeck at high-temperatures. This corresponds to $ZT > 2.5$ with measured thermal conductivity and theoretical electrical conductivity. Finally, demonstrated fast Seebeck mapping with a novel multi-probe scanning Seebeck system. This is now used by BSST (Gentherm) to study the uniformity of variety of TE materials. Finally performed a detailed cost/efficiency trade off analysis for TE power generation and first analytical calculation of stress in multi-leg TE modules. The new model shows that the shearing stress under temperature gradient can be significantly reduced with low fractional area coverage of TE elements.

Enter List of papers submitted or published that acknowledge ARO support from the start of the project to the date of this printing. List the papers, including journal references, in the following categories:

(a) Papers published in peer-reviewed journals (N/A for none)

<u>Received</u>	<u>Paper</u>
05/30/2013 13.00	Kevin C. See, Joseph P. Feser, Cynthia E. Chen, Arun Majumdar, Jeffrey J. Urban, Rachel A. Segalman. Water-Processable Polymer?Nanocrystal Hybrids for Thermoelectrics, Nano Letters, (11 2010): 4664. doi: 10.1021/nl102880k
05/30/2013 24.00	Ekaterina Selezneva, Laura E. Clinger, Ashok T. Ramu, Gilles Pernot, Trevor E. Buehl, Tela Favaloro, Je-Hyeong Bahk, Zhixi Bian, John E. Bowers, Joshua M. O. Zide, Ali Shakouri. Thermoelectric Transport in InGaAs with High Concentration of Rare-Earth TbAs Embedded Nanoparticles, Journal of Electronic Materials, (04 2012): 0. doi: 10.1007/s11664-012-2097-3
05/30/2013 23.00	Hsinyi Lo, Rajeev J. Ram. Submicron Mapping of Thermal Conductivity of Thermoelectric Thin Films, Journal of Electronic Materials, (12 2011): 0. doi: 10.1007/s11664-011-1872-x
05/30/2013 22.00	Je-Hyeong Bahk, Ramin Banan Sadeghian, Zhixi Bian, Ali Shakouri. Seebeck Enhancement Through Miniband Conduction in III-V Semiconductor Superlattices at Low Temperatures, Journal of Electronic Materials, (02 2012): 0. doi: 10.1007/s11664-012-1917-9
05/30/2013 19.00	Zhixi Bian, Mona Zebarjadi, Joshua M. O. Zide, Hong Lu, Dongyan Xu, Joseph P. Feser, Gehong Zeng, Arun Majumdar, Arthur C. Gossard, Ali Shakouri, John E. Bowers, Je-Hyeong Bahk. Thermoelectric figure of merit of $(\text{In}_{0.53}\text{Ga}_{0.47}\text{As})_{0.8}(\text{In}_{0.52}\text{Al}_{0.48}\text{As})_{0.2}$ III-V semiconductor alloys, Physical Review B, (06 2010): 0. doi: 10.1103/PhysRevB.81.235209
05/30/2013 21.00	Ramin Banan Sadeghian, Je-Hyeong Bahk, Zhixi Bian, Ali Shakouri. Calculation of Nonlinear Thermoelectric Coefficients of $\text{InAs}_{1-x}\text{Sb}_x$ Using Monte Carlo Method, Journal of Electronic Materials, (12 2011): 0. doi: 10.1007/s11664-011-1858-8
05/30/2013 20.00	Ashok T. Ramu, Laura E. Cassels, Nathan H. Hackman, Hong Lu, Joshua M. O. Zide, John E. Bowers. Rigorous calculation of the Seebeck coefficient and mobility of thermoelectric materials, Journal of Applied Physics, (04 2010): 0. doi: 10.1063/1.3366712
05/30/2013 18.00	Laura E. Clinger, Gilles Pernot, Trevor E. Buehl, Peter G. Burke, Arthur C. Gossard, Christopher J. Palmstrom, Ali Shakouri, Joshua M. O. Zide. Thermoelectric properties of epitaxial TbAs:InGaAs nanocomposites, Journal of Applied Physics, (05 2012): 0. doi: 10.1063/1.4711095
05/30/2013 17.00	Pankaj Jha, Timothy D. Sands, Laura Cassels, Philip Jackson, Tela Favaloro, Benjamin Kirk, Joshua Zide, Xianfan Xu, Ali Shakouri. Cross-plane electronic and thermal transport properties of p-type $\text{La}_{0.67}\text{Sr}_{0.33}\text{MnO}_3/\text{LaMnO}_3$ perovskite oxide metal/semiconductor superlattices, Journal of Applied Physics, (09 2012): 0. doi: 10.1063/1.4754514
05/30/2013 16.00	Ashok T. Ramu, Laura E. Clinger, Pernell B. Dongmo, Jeffrey T. Imamura, Joshua M. O. Zide, John E. Bowers. Incompatibility of standard III-V compound semiconductor processing techniques with terbium-doped InGaAs of high terbium concentration, Journal of Vacuum Science & Technology A: Vacuum, Surfaces, and Films, (04 2012): 0. doi: 10.1116/1.3701951
05/30/2013 15.00	Je-Hyeong Bahk, Parthiban Santhanam, Zhixi Bian, Rajeev Ram, Ali Shakouri. Resonant carrier scattering by core-shell nanoparticles for thermoelectric power factor enhancement, Applied Physics Letters, (01 2012): 0. doi: 10.1063/1.3673615

- 08/31/2011 11.00 J. M. O. Zide, J.-H. Bahk, R. Singh, M. Zebarjadi, G. Zeng, H. Lu, J. P. Feser, D. Xu, S. L. Singer, Z. X. Bian, A. Majumdar, J. E. Bowers, A. Shakouri, A. C. Gossard. High efficiency semimetal/semiconductor nanocomposite thermoelectric materials, *Journal of Applied Physics*, (12 2010): 123702. doi: 10.1063/1.3514145
- 08/31/2011 12.00 Ali Shakouri, Arun Majumdar, Mercouri G. Kanatzidis, Christopher J. Vineis. Nanostructured Thermoelectrics: Big Efficiency Gains from Small Features, *Advanced Materials*, (09 2010): 3970. doi: 10.1002/adma.201000839
- 08/31/2011 10.00 Laura E. Cassels, Nathan H. Hackman, Ashok T. Ramu, Hong Lu, Joshua M. O. Zide, John E. Bowers. Thermoelectric transport in the coupled valence-band model, *Journal of Applied Physics*, (02 2011): 33704. doi: 10.1063/1.3537826
- 08/31/2011 9.00 Peter G. Burke, Hong Lu, Nicholas G. Rudawski, Susanne Stemmer, Arthur C. Gossard, Je-Hyeong Bahk, John E. Bowers. Electrical properties of Er-doped In_{0.53}Ga_{0.47}As, *Journal of Vacuum Science & Technology B: Microelectronics and Nanometer Structures*, (05 2011): 1071. doi: 10.1116/1.3559480
- 08/31/2011 8.00 Gilles Pernot, Ali Shakouri, Chelsea R. Haughn, Matthew F. Doty, Joshua M. O. Zide, Trevor E. Buehl, Peter G. Burke, Chris J. Palmstrom, Art C. Gossard, Laura E. Cassels. Growth and characterization of TbAs:GaAs nanocomposites, *Journal of Vacuum Science & Technology B: Microelectronics and Nanometer Structures*, (02 2011): 1071. doi: 10.1116/1.3555388
- 08/31/2011 7.00 Mona Zebarjadi, Keivan Esfarjani, Zhixi Bian, Ali Shakouri. Low-Temperature Thermoelectric Power Factor Enhancement by Controlling Nanoparticle Size Distribution, *Nano Letters*, (01 2011): 225. doi: 10.1021/nl103581z
- 08/31/2011 5.00 Ali Shakouri. Recent Developments in Semiconductor Thermoelectric Physics and Materials, *Annual Review of Materials Research*, (08 2011): 399. doi: 10.1146/annurev-matsci-062910-100445
- 08/31/2011 6.00 Peter G. Burke, Hong Lu, Arthur C. Gossard, Gehong Zeng, Ashok T. Ramu, Je-Hyeong Bahk, John E. Bowers. Semimetal/Semiconductor Nanocomposites for Thermoelectrics, *Advanced Materials*, (05 2011): 2377. doi: 10.1002/adma.201100449
- 08/31/2011 4.00 Je-Hyeong Bahk, Zhixi Bian, Mona Zebarjadi, Parthiban Santhanam, Rajeev Ram, Ali Shakouri. Thermoelectric power factor enhancement by ionized nanoparticle scattering, *Applied Physics Letters*, (08 2011): 72118. doi: 10.1063/1.3625950
- 12/07/2013 25.00 E. Suhir, A. Shakouri. Assembly Bonded at the Ends: Could Thinner and Longer Legs Result in a Lower Thermal Stress in a Thermoelectric Module Design?, *Journal of Applied Mechanics*, (11 2012): 61010. doi: 10.1115/1.4006597
- 12/07/2013 26.00 Kazuaki Yazawa, Ali Shakouri. Scalable Cost/Performance Analysis for Thermoelectric Waste Heat Recovery Systems, *Journal of Electronic Materials*, (04 2012): 1845. doi: 10.1007/s11664-012-2049-y
- 12/07/2013 27.00 E. Suhir, A. Shakouri. Predicted Thermal Stress in a Multileg Thermoelectric Module (TEM) Design, *Journal of Applied Mechanics*, (01 2013): 21012. doi: 10.1115/1.4007524
- 12/07/2013 28.00 Polina V. Burmistrova, Jesse Maassen, Tela Favaloro, Bivas Saha, Shuaib Salamat, Yee Rui Koh, Mark S. Lundstrom, Ali Shakouri, Timothy D. Sands. Thermoelectric properties of epitaxial ScN films deposited by reactive magnetron sputtering onto MgO(001) substrates, *Journal of Applied Physics*, (04 2013): 153704. doi: 10.1063/1.4801886
- 12/07/2013 29.00 Pankaj Jha, Timothy D. Sands, Philip Jackson, Cory Bomberger, Tela Favaloro, Stephen Hodson, Joshua Zide, Xianfan Xu, Ali Shakouri. Cross-plane thermoelectric transport in p-type La_{0.67}Sr_{0.33}MnO₃/LaMnO₃ oxide metal/semiconductor superlattices, *Journal of Applied Physics*, (05 2013): 193702. doi: 10.1063/1.4804937

TOTAL: 25

Number of Papers published in peer-reviewed journals:

(b) Papers published in non-peer-reviewed journals (N/A for none)

<u>Received</u>	<u>Paper</u>
-----------------	--------------

TOTAL:

Number of Papers published in non peer-reviewed journals:

(c) Presentations

1. Ali Shakouri, Invited talk "Design of High Performance, Robust and Low Cost Thermoelectric Modules," MRS Fall Meeting, Symposium B, Boston, MA; November 2012
2. Ali Shakouri, Invited talk "Nanoscale Electrothermal Energy Transport," Cornell University; November 2012
3. Ali Shakouri, Invited talk "Cost Efficiency Trade Off in Nanostructured Thermoelectric Systems," American Vacuum Society 59th Annual International Symposium, Tampa, Florida; 29 October 2012
4. Ali Shakouri, Invited Talk, "Nanostructured thermoelectric energy conversion and refrigeration devices," Device Research Conference, Penn State University; June 2012
5. Ali Shakouri, Invited Talk, "Nanostructured materials for thermoelectric conversion," SPIE (International Society for Optics and Photonics) Defense, Security + Sensing, Baltimore, MD; April 2012
6. Ali Shakouri, Invited Talk, "Nanostructured thermoelectric materials for waste heat recovery," Symposium on Nanomaterials for Energy, Purdue University; April 2012
7. Ali Shakouri, Invited Talk, "Linear and Non-linear Thermoelectric Transport for Waste Heat Recovery," BNNI (Berkeley Nanosciences and Nanoengineering Institute) Seminar, Berkeley, CA; February 2012
8. Ali Shakouri, Invited Talk, "Symposium W: Phonons in Nanomaterials-Theory, Experiments, and Applications," 2011 MRS (Materials Research Society) Fall Meeting Symposium, Boston, MA; November 2011
9. Ali Shakouri, Invited Talk, "Nanostructured thermoelectric materials for waste head recovery applications and for microfrigeration," Princeton University, November 2011
10. (invited) "Semimetal/semiconductor nanostructured composites for thermoelectric applications", Hong Lu, University of Texas, Austin, Texas, June 2011.
11. (invited) "Semimetal/semiconductor nanostructured composites for thermoelectrics" Hong Lu, University of Notre Dame, Indiana, March 2011.
12. (invited) A. Shakouri, "Material tradeoffs in direct thermal to electric energy conversion systems," American Physical Society March Meeting, Symposium on Materials for Energy, Dallas, TX, March 2011
13. J. M. O. Zide, "Enhancing Efficiency in Thermoelectrics with MBE-grown Tb(Er)As/InGaAs Nanocomposites," Presented at North American Conference on MBE, San Diego, CA, 2011.
14. J. M. O. Zide, "Novel Semiconductors and Epitaxial Nanocomposites for Applications in Thermoelectrics, Terahertz, and Optoelectronics" Presented at National Institute of Standards and Technology, Boulder, CO, 2011.
15. J. M. O. Zide, "Novel Semiconductor and Epitaxial Nanocomposite Materials for Energy Conversion Applications" Presented at Millersville University, Millersville, PA (2011).
16. R. Amatya and R.J. Ram, "Trend for thermoelectric materials and their earth abundance," International Thermoelectrics Conference, 2011.
17. Laura E. Cassels, Ashok T. Ramu, Gilles Pernot, Trevor E. Buehl, Peter G. Burke, Art C. Gossard, Chris J. Palmstrøm, Ali Shakouri, John E. Bowers,, "Improving Thermoelectric Power Generation Efficiency with Epitaxial TbAs/III-V Nanocomposites." the 2011 Electronic Materials Conference, Santa Barbara, CA (2011).
18. Hong Lu, Peter Burke, Nathan H. Hackman, John E. Bowers, Arthur C. Gossard, "Thermoelectric properties of ErSb:In_xGa_{1-x}Sb thin films grown by MBE", Electronic Materials Conference 2011, Santa Barbara, CA, June 22-24, 2011
19. P. G. Burke, J. E. Bowers, and A. C. Gossard, "Nanoparticle size dependence of the electrical, thermal, and optical properties of Er-doped In_{0.53}Ga_{0.47}As," Electronic Materials Conference 2011, Santa Barbara, CA, June 22-24, 2011
20. Zhixi Bian, Je-Hyeong Bahk, Mona Zebarjadi, Ali Shakouri, Parthiban Santhanam and Rajeev J. Ram "Effects of Nanoparticle Resonant States on Thermoelectric Transport," Materials Research Symposium, April 2011
21. Burmistrova, P., Schroeder, J., Wortman, R., Jackson, P., Shakouri, A., & Sands, T. (2011). Microstructure and Thermoelectric Properties of Nitride Metal/Semiconductor Superlattices for High-Temperature Energy Conversion. 30th International Conference on Thermoelectrics (ICT 2011).

22. T. Onishi, K. J. Norris, E. Colman, V. Wong, A. Shakouri, G. S. Tompa, N. P. Kobayashi, "MOCVD growth of erbium monoantimonide thin films and nanocomposites for thermoelectrics", ICT 2011.
23. Laura E. Cassels, Gilles Pernot, Trevor E. Buehl, Art C. Gossard, Chris J. Palmstrøm, Ali Shakouri, Joshua M. O. Zide, "Improving Thermoelectric Power Generation Efficiency with epitaxial TbAs/III-V Nanocomposites." ICT 2011.
24. L. Cassels, P. Dongmo, A. Ramu, G. Pernot, T. Buehl, A. Gossard, A. Shakouri, C. Palmstrøm, J. Bowers, J. M. O. Zide, "Enhancing Efficiency in Thermoelectrics with MBE-grown Tb(Er)As/InGaAs Nanocomposites," North American Conference on Molecular Beam Epitaxy, San Diego, CA (2011).
25. Schroeder JL, Ewoldt D, Burmistrova P, Wortman R, and Sands TD, "Laminated Nanostructured Metal/Semiconductor Superlattices for Bulk-like Thermionic Energy Conversion Devices," AMN-5 (Advanced Materials and Nanotechnology Conference), Wellington, New Zealand, February 11th, (2011).
26. J. M. O. Zide, Optical, electrical, and thermal properties of TbAs:(In)GaAs Nanocomposites, Workshop on embedded nanoparticles, Santa Barbara, CA (2011).
27. AMN-5 2011 (Advanced Materials and Nanotechnology Conference), Laminated Nanostructured Metal/Semiconductor Superlattices for Bulk-like Thermionic Energy Conversion Devices, Presenter: Jeremy L. Schroeder
28. A. Shakouri, Invited Talk, "Transient charge and energy transport in thermoelectric devices," Workshop on New Trends in Nonlinear Dynamics: Heat Control and Thermoelectricity (HEAT 2010), Erice, Italy; October 2010
29. A. Shakouri, Invited Talk, "Thermoelectric transport in nanostructured materials," Workshop on Electronic Transport in Nanoengineered Materials, University of Chicago, IL; September 2010
30. Hong Lu, Peter Burke, Gehong Zeng, John Bowers, Arthur C. Gossard, "MBE grown ErSb:InxGa1-xSb and its application in thermoelectrics", 27th North American Molecular Beam Epitaxy Conference, Breckenridge, CO, September 27, 2010
31. P. G. Burke, H. Lu, N. G. Rudawski, S. Stemmer, J.-H. Bahk, T. Favaloro, A. Shakouri, J. E. Bowers, and A. C. Gossard, "Electrical and optical properties of nanoparticle thermoelectric power generation materials," 27th North American Molecular Beam Epitaxy Conference, Breckenridge, CO, September 27, 2010
32. J. M. O. Zide, "Improved Thermoelectric Performance in Epitaxial Metal/Semiconductor Nanocomposites," Army Workshop on Advanced Concepts in Semiconductor Materials and Devices for Energy Conversion, Beltsville, MD (2010).
33. J. M. O. Zide, "Improved Thermoelectric Performance in Epitaxial Metal/Semiconductor Nanocomposites," Advanced Concepts in Semiconductor Materials and Devices for Energy Conversion, Beltsville, MD (2010).
34. P.V. Burmistrova, J.L. Schroeder, D.A. Ewoldt, R. Amatya, R. Ram, and T.D. Sands, "Nitride Metal/Semiconductor Superlattices for High-Temperature Solid-State Energy Conversion," 2010 MRS Spring Meeting, San Francisco, CA, April 8th (2010).
35. R. Wortman, J. Schroeder, P. Burmistrova, L. Cassels, T. Sands, and J. Zide, "Epitaxial Growth of Transition Metal Nitrides on MgO via DC Magnetron Sputtering," Electronic Materials Conference, June 25th (2010).
36. Schroeder JL, Ewoldt D, Burmistrova P, Wortman R, and Sands TD, "Bulk-like Thermionic Energy Conversion Device Fabricated from Laminated Nanostructured Metal/Semiconductor Superlattices," 2010 Electronic Materials Conference, University of Notre Dame, June 25th (2010).
37. Schroeder JL, Ewoldt D, Burmistrova P, Wortman R, and Sands TD, "Bridging the gap between nano and micro for advanced thermoelectric materials/devices," UGIM 2010 (University Government Industry Micro/Nano Symposium), Purdue University, July 1st (2010).
38. J. M. O. Zide. "Novel Metal/Semiconductor Nanocomposite and Superlattice Materials and Devices for Thermoelectrics" SPIE – Defense, Security, and Sensing. Orlando, FL (2010).
39. J. M. O. Zide, A. Shakouri, and A. Majumdar. "The Use of Nanoparticle Inclusions to Reduce Thermal Conductivity in Thermoelectrics." Advances in Peltier Cooling Workshop, Air Force Research Laboratory, Albuquerque, NM (2009).
40. J. M. O. Zide. "Metal/Semiconductor Nanocomposites and Electron Filtering Effects for Thermoelectric Applications." 8th Pacific Rim Conference on Ceramic and Glass Technology. Vancouver, BC, Canada. (2009).

41. P.V. Burmistrova, J.L. Schroeder, R. Wortman, and T.D. Sands, “Microstructure and Thermoelectric Properties of HfN/ScN Metal/Semiconductor Superlattices for Thermionic Energy Conversion,” Poster N3.9, 2009 MRS Spring Meeting, San Francisco, CA (2009).

42. J. Schroeder, P. Burmistrova, R. Wortman and T.D. Sands, “Alternative Substrates for Metal/Semiconductor Superlattices for Thermionic Energy Conversion, “ L8, 2009 Electronic Materials Conference, Penn. St. University (2009).

43. J. Schroeder, P. Burmistrova, R. Wortman, D. Ewoldt and T. Sands, “Metal/Semiconductor Superlattices on Silicon Substrates for Solid-State Thermionic Energy Conversion Devices, , Z 2.7, 2009 MRS Fall Meeting, Boston, MA, November 30th (2009).

44. R. Wortman, J. Schroeder, P. Burmistrova, T. Sands, M. Zebarjadi, Z. Bian, and A. Shakouri, “Nitride Metal-Semiconductor Superlattices for Solid-State Thermionic Energy Conversion”, American Physics Society March Meeting, Pittsburgh, PA, March (2009).

45. R. Wortman, J. Schroeder, P. Burmistrova, T. Sands, M. Zebarjadi, Z. Bian, and A. Shakouri, “Solid State Thermionic Direct Thermal to Electrical Energy Conversion with Nitride Metal-Semiconductor Superlattices,” International Conference on Thermoelectrics, Freiburg, Germany, July (2009).

Number of Presentations: 45.00

Non Peer-Reviewed Conference Proceeding publications (other than abstracts):

Received Paper

TOTAL:

Number of Non Peer-Reviewed Conference Proceeding publications (other than abstracts):

Peer-Reviewed Conference Proceeding publications (other than abstracts):

Received Paper

TOTAL:

Number of Peer-Reviewed Conference Proceeding publications (other than abstracts):

(d) Manuscripts

Received

Paper

- 08/31/2011 1.00 Je-Hyeong Bahk, Ramin Banan Sadeghian, Zhixi Bian, Ali Shakouri. Seebeck enhancement through miniband conduction in III-V semiconductor superlattices at low temperatures, Journal of Electronic Materials (08 2011)
- 08/31/2011 2.00 Ramin Banan Sadeghian, Je-Hyeong Bahk, Zhixi Bian, Ali Shakouri. Calculation of Nonlinear Thermoelectric Coefficients of InAs_{1-x}Sb_x using Monte Carlo Method, Journal of Electronic Materials (08 2011)
- 08/31/2011 3.00 Ekaterina Selezneva, Laura Cassels, Ashok Ramu, Gilles Pernot, Tela Favaloro, Je-Hyeong Bahk, Mona Zebarjadi, Zhixi Bian, John Bowers, Joshua Zide, Ali Shakouri. Thermoelectric transport in InGaAs with high concentration of rare-earth TbAs embedded nanoparticles, Journal of Electronic Materials (08 2011)
- 08/31/2011 14.00 Hsinyi Lo, Rajeev J. Ram. Sub-micron Mapping Thermal Conductivity of Thermoelectric Thin Films, Journal of Electronic Materials (08 2011)

TOTAL: 4

Number of Manuscripts:

Books

Received

Paper

TOTAL:

Patents Submitted

"EFFECTIVE AND SCALABLE SOLAR ENERGY COLLECTION AND STORAGE," Kazuaki YAZAWA, Zhixi BIAN, Ali SHAKOURI

Patents Awarded

(1) United States Patent Application, EFS ID 8939363, LAMINATED THIN FILM METAL-SEMICONDUCTOR MULTILAYERS FOR THERMOELECTRICS, (Jeremy L. Schroeder and Timothy D. Sands)

(2) Provisional United States Patent, EFS ID- 9611658, P-TYPE LANTHANUM STRONTIUM MANGANATE/LANTHANUM MANGANATE PEROVSKITE OXIDE METAL/SEMICONDUCTOR SUPERLATTICES FOR THERMOELECTRICS, (Pankaj Jha and Timothy D. Sands)

Awards

Joshua M. O. Zide: 2011 North American Molecular Beam Epitaxy Young Investigator

Graduate Students

<u>NAME</u>	<u>PERCENT SUPPORTED</u>	Discipline
Peter Burke	0.50	
Robert Wortman	0.58	
Philip Jackson	0.50	
Tela Favaloro	0.50	
Polina Burmistrova	1.00	
Pernell Dongmo	0.50	
Laura Cassels	1.00	
Reja Amatya	1.00	
Ashok T. Ramu	0.45	
Oxana Pantchenko	0.75	
FTE Equivalent:	6.78	
Total Number:	10	

Names of Post Doctorates

<u>NAME</u>	<u>PERCENT SUPPORTED</u>
Je-Hyeong Bahk	0.25
Gilles Pernot	0.25
Katey Lo	0.80
FTE Equivalent:	1.30
Total Number:	3

Names of Faculty Supported

<u>NAME</u>	<u>PERCENT SUPPORTED</u>	National Academy Member
Zhixi Bian	0.70	
Nobby Kobayashi	0.10	
Joshua Zide	0.15	
Rajeev Ram	0.05	
John Bowers	0.05	Yes
Art Gossard	0.05	Yes
Ali Shakouri	0.30	
FTE Equivalent:	1.40	
Total Number:	7	

Names of Under Graduate students supported

<u>NAME</u>	<u>PERCENT SUPPORTED</u>	Discipline
Vernon Wong	0.25	
Danny Tate	0.10	
Nathan H. Hackman	0.20	
FTE Equivalent:	0.55	
Total Number:	3	

Student Metrics

This section only applies to graduating undergraduates supported by this agreement in this reporting period

The number of undergraduates funded by this agreement who graduated during this period: 3.00

The number of undergraduates funded by this agreement who graduated during this period with a degree in science, mathematics, engineering, or technology fields:..... 3.00

The number of undergraduates funded by your agreement who graduated during this period and will continue to pursue a graduate or Ph.D. degree in science, mathematics, engineering, or technology fields:..... 0.00

Number of graduating undergraduates who achieved a 3.5 GPA to 4.0 (4.0 max scale):..... 3.00

Number of graduating undergraduates funded by a DoD funded Center of Excellence grant for Education, Research and Engineering:..... 0.00

The number of undergraduates funded by your agreement who graduated during this period and intend to work for the Department of Defense 0.00

The number of undergraduates funded by your agreement who graduated during this period and will receive scholarships or fellowships for further studies in science, mathematics, engineering or technology fields: 0.00

Names of Personnel receiving masters degrees

NAME

Laura Cassels

Philip Jackson

Total Number: 2

Names of personnel receiving PHDs

NAME

Ashok T. Ramu

Reja Amatya

Robert Wortman

Polina Burmistrova

Jeremy Schroeder

Joe Feser

Oxana Pantchenko

Total Number: 7

Names of other research staff

NAME

PERCENT SUPPORTED

Dustin Kendig 0.30

Jeremy Schroeder 0.33

Ashok T. Ramu 0.50

Brenna Candelaria 0.10

Hong Lu 0.50

Kaz Yazawa 0.15

FTE Equivalent: 1.88

Total Number: 6

Sub Contractors (DD882)

Inventions (DD882)

5 LAMINATED THIN FILM METAL-SEMICONDUCTOR MULTILAYERS FOR THERMOELECTRICS

Patent Filed in US? (5d-1) Y

Patent Filed in Foreign Countries? (5d-2) N

Was the assignment forwarded to the contracting officer? (5e) N

Foreign Countries of application (5g-2):

5a: Timothy D. Sands

5f-1a: Purdue University

5f-c: West State St.

West Lafayette IN 47907-205

5 P-TYPE LANTHANUM STRONTIUM MANGANATE/LANTHANUM MANGANATE PEROVSKITE OXIDE METAL/

Patent Filed in US? (5d-1) Y

Patent Filed in Foreign Countries? (5d-2) N

Was the assignment forwarded to the contracting officer? (5e) N

Foreign Countries of application (5g-2):

5a: Timothy D. Sands

5f-1a: Purdue University

5f-c: West State St.

West Lafayette IN 47907-205

Scientific Progress

See Attachment

Technology Transfer

Metal-Semiconductor Nanocomposites for High Efficiency Thermoelectric Power Generation

Grant number - W911NF-08-1-0347

Final Report July 2013

DARPA Program Manager: Brian Holloway
Army Program Monitor: John Prater

Ali Shakouri (PI) UC Santa Cruz

Participants:

<i>UC Santa Cruz</i>	<i>Nobby Kobayashi, Zhixi Bian</i>
<i>UC Santa Barbara</i>	<i>John Bowers, Art Gossard</i>
<i>UC Berkeley</i>	<i>Arun Majumdar</i>
<i>MIT</i>	<i>Rajeev Ram</i>
<i>Purdue</i>	<i>Tim Sands</i>
<i>Delaware</i>	<i>Josh Zide</i>
<i>BSST</i>	<i>Lon Bell</i>

Some highlights of achievement:

- Demonstrated $ZT \sim 1.6-1.7$ at 840K (0.5% ErAs:InGaAs) –UCSB/UCSC/Berkeley
- Demonstrated $ZT \sim 1.8$ at 780K (0.12 % ErAs:InGaAs) –UCSB/UCSC/Berkeley
- Giant cross-plane Seebeck coefficients of 2560 $\mu\text{V/K}$ at room temperature and 16,640 $\mu\text{V/K}$ at 360 K, and extremely low room temperature thermal conductivity of 0.92 W/mK achieved for $\text{La}_{0.67}\text{Sr}_{0.33}\text{MgO}_3/\text{LaMnO}_3$ perovskite oxide metal/semiconductor superlattices – Purdue/UCSC
- Epitaxial ScN film deposited by reactive DC magnetron sputtering on MgO(001) substrate: measured $ZT \sim 0.3$ at 800 K, power factor of 33~35 $24 \mu\text{W/cmK}^2$ at 600 ~ 840 K, and cross-plane thermal conductivity of 8.3 W/mK at 800 K. Excellent agreement with the first principle calculations –Purdue/UCSC
- Successful electron transport modeling for ErAs:InGaAs with nanoparticle scattering calculations – explains temperature dependent Seebeck coefficient and mobility without fitting parameters (UCSC/Purdue)
- High temperature characterization of 0.1-5% TbAs:InGaAs, ZT of 1.04 at 600K for 0.8% TbAs:InGaAs (power factor enhancement: 83%)–Delaware/UCSB/Berkeley
- ErSb:In_xGa_{1-x}Sb optimization: p-type: for $x=0.69$, highest measured $ZT=0.57$ at 530K and highest measured power factor: 24 $\mu\text{W/cmK}^2$ at 455 K. –UCSB/Berkeley
- Demonstrated range of possible ErSb nanostructures in GaSb including highly regular nanowires – UCSB
- Observation of thermionic emission in nitride superlattices –Purdue/UCSC
- Theoretical optimization of nanoparticle size and potential profile, power factor enhancement 50%~90% for InGaAs and InGaSb based materials –UCSC
- Excellent agreement between theory and experiment for ErSb:InGaSb thermal conductivity – Berkeley/UCSB
- Fast Seebeck mapping with a novel multi-probe scanning Seebeck system (used to study the sample uniformity for bulk grown rare-earth/III-V's); Correlation with extensive composition analysis using EDS – BSST/Purdue
- First measurements of Seebeck for nitride superlattice (130uV/K at 700K). Matches theoretical Seebeck at high-T. This corresponds to $ZT > 2.5$ with measured thermal conductivity and theoretical electrical conductivity –MIT/Purdue
- Consistent thermal conductivity measurements of nitrides (Z-meter, thermorefectance, 3w); and ZT of ErAs:InGaAlAs –MIT/UCSB/UCSC/Berkeley
- Technology impact (cost/efficiency trade off analysis for TE power generation) –UCSC
- First analytical calculation of stress in multi-leg TE modules. -UCSC
- Theoretical prediction that the shearing stress under temperature gradient can be significantly reduced with low fractional area coverage of TE elements –UCSC/Purdue

In the following, we will describe the main technical achievements by each team which covers all aspects of material growth, modeling and simulations, characterization, device fabrication, efficiency measurements and the system requirements.

1. Electron transport modeling of metal-semiconductor nanocomposites (UCSC/Purdue)

A. Electron transport modeling and optimization in n-type ErAs:InGaAs

We have successfully measured ZT of 0.5% ErAs:InGaAs to be ~ 1.6 - 1.7 at 840 K, and ZT of 0.12 % ErAs:InGaAs to be ~ 1.8 at 780 K. As shown in Fig. 1, the ZT values increased with temperature from room temperature to 840 K, which indicates that the transport in this nanocomposites is still unipolar (electron) with intrinsic carriers much smaller than the doping level ($1.7 \times 10^{18} \text{ cm}^{-3}$) up to this high temperature due to the fairly large band gap of InGaAs (740 meV). ZT ~ 1.6 at 840 K and ZT ~ 1.8 at 780 K are much higher than ZT ~ 1.33 at 800 K that was previously obtained from 0.6% ErAs:InGaAlAs (20% Al). This is mainly due to the higher electron mobility in InGaAs host matrix than that in InGaAlAs: alloying with Al increases both band gap and effective mass of electron in InGaAs. We included the composition-dependent band structures parameters as well as the modified phonon and alloy scattering parameters in the modeling to explain the thermoelectric properties of this material. For example, we adapted the literature values of electron effective mass for $(\text{InGaAs})_{1-x}(\text{InAlAs})_x$ lattice-matched to InP, which is $(0.041*(1-x)+0.075*x)m_0$, in our multi-band Boltzmann transport model. Also the nanoparticle scattering rate calculated by the partial wave method has been added to the total scattering rate to fit the electrical conductivity and Seebeck coefficient as a function of temperature for ErAs:InGa(Al)As.

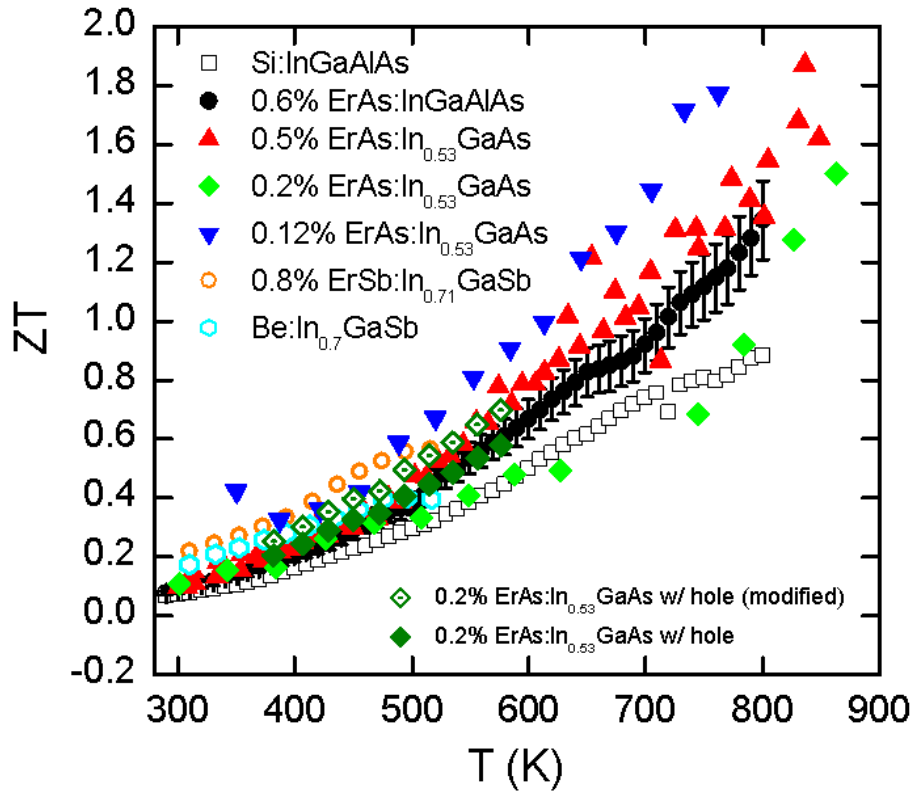


Figure 1. Temperature dependent ZT of n-type ErAs:InGaAs, ErAs:InGaAlAs and the reference sample Si:InGaAlAs and p-type ErSb:InGaSb and the reference sample Be:InGaSb.

Fig. 2 presents the electrical conductivity of 0.5% ErAs:InGaAs in comparison with those of 0.6% ErAs:InGaAlAs (20% Al) and Si-doped InGaAlAs (20% Al). Due to its lighter effective mass, the electrical conductivity of 0.5% ErAs:InGaAs was higher than those of InGaAlAs at similar doping levels. The carrier density was $\sim 1.7 \times 10^{18} \text{ cm}^{-3}$ for 0.5% ErAs:InGaAs, only slightly increasing with temperature, indicating the activation energy of the ErAs doping is a very small positive value. For comparison, 0.6% ErAs:InGaAs showed the carrier density more rapidly increasing from $8 \times 10^{17} \text{ cm}^{-3}$ at 300 K to $2.0 \times 10^{18} \text{ cm}^{-3}$ at 840 K. The Si-doped control sample has the constant electron density at $1.9 \times 10^{18} \text{ cm}^{-3}$ in this temperature range. Even though their carrier densities were similar, 0.5% ErAs:InGaAs showed higher electrical conductivity than the control InGaAlAs sample due to higher mobility: 14% higher at 300 K and 30% higher at 840 K. The nanoparticle scattering reduced mobility in the ErAs:InGaAs sample slightly ($\sim 5\%$) from its control, Si-doped InGaAs. On the other hand, 0.6% ErAs:InGaAlAs showed lower electrical conductivity than those of the other two samples even though the carrier density was higher. This is because its mobility was largely suppressed by the nanoparticle scattering and the impurity scattering.

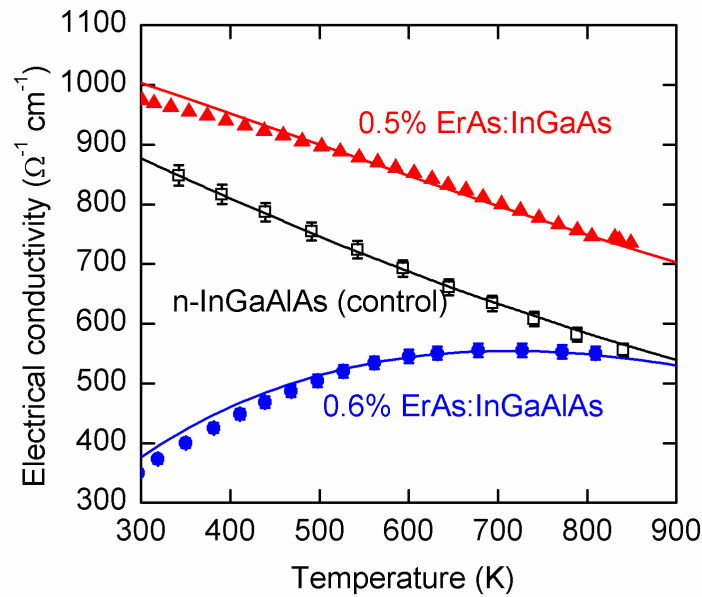


Figure 2. Electrical conductivity as a function of temperature for 0.5 % ErAs:InGaAs and 0.6 % ErAs:InGaAlAs (20% Al). For comparison, the values of Si-doped n-type control InGaAlAs are also shown. Symbols are measured values, and solid curves are theoretical calculations.

The Seebeck coefficients, shown in Figure 3, increased with increasing temperature for all the three samples. The increasing rate of Seebeck coefficient with temperature was smallest for 0.6% ErAs:InGaAlAs because the carrier density increased with temperature. The Seebeck coefficients of 0.5% ErAs:InGaAs and the Si-doped InGaAlAs did not look very different, almost identical within the error bars for similar carrier densities. This is a clear evidence of the similar band structures with good quality of crystals for these two samples. The 0.6% ErAs:InGaAlAs showed higher Seebeck coefficients than the other two samples due to the lower carrier densities. At higher temperatures, the nanoparticle scattering also helped the Seebeck coefficient stay high for 0.6% ErAs:InGaAlAs compared to the control sample at the equivalent doping level. Even though the Seebeck coefficient of

0.6% ErAs:InGaAlAs was higher than that of 0.5% ErAs:InGaAs at 840 K, its power factor was lower because of the lower conductivity.

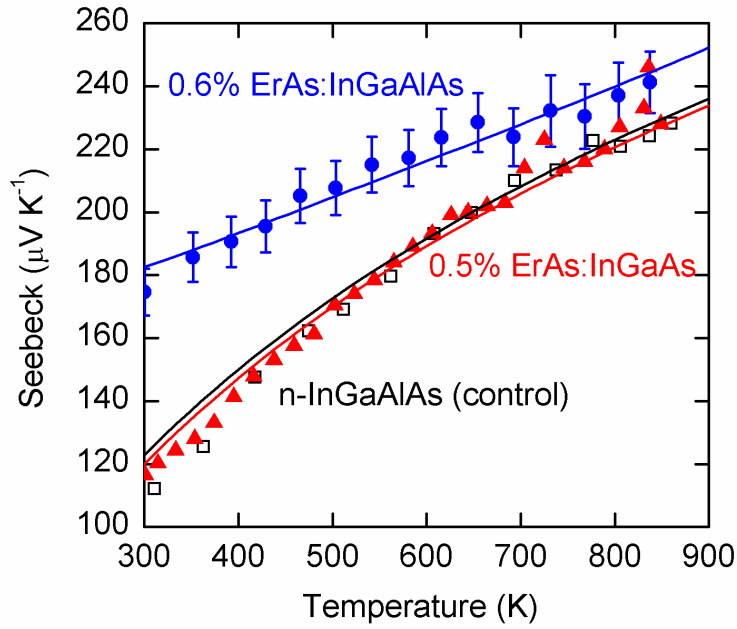


Figure 3. Seebeck coefficient as a function of temperature for 0.5 % ErAs:InGaAs and 0.6 % ErAs:InGaAlAs (20% Al). For comparison, the values of Si-doped n-type control InGaAlAs are also shown. Symbols are measured values, and curves are theoretical fittings.

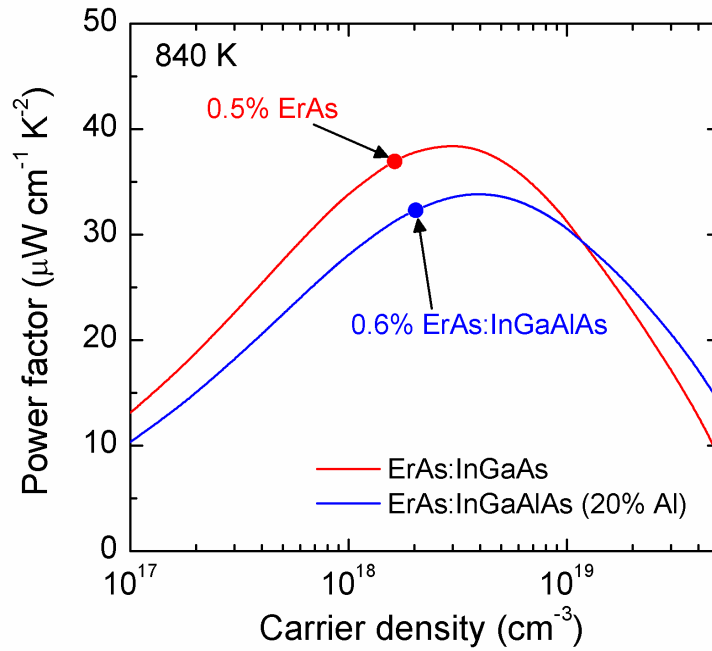


Figure 4. Calculated power factor as a function of carrier density at 840 K for ErAs:InGaAs and ErAs:InGaAlAs (20% Al). Dots are experimental data for 0.5%

Based on the modeling and fitting with experimental data, we calculated the power factor as a function of carrier density at 840 K for both ErAs:InGaAs and ErAs:InGaAlAs. The results are shown in Fig. 4. The measured data points are shown as filled dots in the figure. It is shown that the two samples are near optimal, with their power factors only a few % lower than the maximum power factors predicted by the theory. This well-designed power factor is the result of our previous experience with this material system and successful modeling. In terms of power factor, InGaAs host matrix is a better choice than its Al alloys.

B. Improvement of ZT in p-type ErSb:InGaSb

Base on the $\text{In}_x\text{Ga}_{1-x}\text{Sb}$ growth condition optimization we achieved during DARPA phase I, we have been focused on achieving high quality $\text{In}_x\text{Ga}_{1-x}\text{Sb}$ films codoped with Er and Be in order to obtain a higher ZT. A series of 2 μm thick ErSb:p- $\text{In}_x\text{Ga}_{1-x}\text{Sb}$ with different In compositions were grown. The In compositions in these samples were intended to be 10%, 30%, 50% and 70%. The actual values are calculated from the XRD data and they vary slightly on the samples grown at different times.

High quality MBE-grown films insure the accurate thermal conductivity measurement by three omega method. Figure 16 (section on thermal conductivity) shows the temperature dependent thermal conductivity of a series of $\text{In}_x\text{Ga}_{1-x}\text{Sb}$ samples with and without ErSb incorporation measured by Joe Feser and Dongyan Xu at UC Berkeley. A clear reduction in thermal conductivity by ErSb incorporation is demonstrated in samples with different In compositions. Thermal conductivity reduction by alloy scattering is also demonstrated as the In composition increases. Most of these samples were measured up to 800 K without indication of degradation. Data up to 600 K are shown here because the Seebeck coefficient and electrical conductivity measurements have been performed up to 600 K.

The ErSb concentration in these samples is kept around 0.8% by volume. The figure-of-merit ZT calculated at room temperature for these samples shows an enhancement of more than 2 times from $\text{In}_{0.15}\text{Ga}_{0.85}\text{Sb}$ ($\text{ZT}=0.076$) to ErSb: $\text{In}_{0.69}\text{Ga}_{0.31}\text{Sb}$ ($\text{ZT}=0.168$). With continuous optimization in overall doping levels and ErSb concentration, the ZT can be further improved. We selected the best room temperature performance samples, which have $\sim 70\%$ In, and passivated them with $\text{SiN}_x/\text{SiO}_2$ followed by (Pt/Ti/Pt/Au) metallization for high temperature measurement. The temperature dependent ZT of Be doped $\text{In}_{0.7}\text{Ga}_{0.3}\text{Sb}$ and ErSb:p $\text{In}_{0.69}\text{Ga}_{0.31}\text{Sb}$ are shown in Fig. 2 as a comparison to the other Er-based thermoelectric materials. Substrate effect started to show up when the temperature was higher than 520K so the data for p-type ErSb: $\text{In}_{0.69}\text{Ga}_{0.31}\text{Sb}$ and $\text{In}_{0.7}\text{Ga}_{0.3}\text{Sb}$ are only showed up to that temperature. With careful substrate removal and transfer, we will be able to measure the thermoelectric properties on these p-type antimonide thermoelectric materials up to a higher temperature therefore a higher ZT is still very promising.

Theoretical calculation shows that the n-type $\text{In}_x\text{Ga}_{1-x}\text{Sb}$ has an optimized ZT with $\sim 70\%$ In. Since we have succeeded in growing high In composition films, we will be able to dope these relevant $\text{In}_x\text{Ga}_{1-x}\text{Sb}$ with Te and optimize the thermoelectric properties in the near future.

2. Cross-plane thermoelectric properties of perovskite oxide metal/semiconductor superlattices (Purdue/UCSC)

The cross-plane thermoelectric transport properties of $\text{La}_{0.67}\text{Sr}_{0.33}\text{MnO}_3$ (LSMO)/ LaMnO_3 (LMO) oxide metal/semiconductor superlattices were investigated. The LSMO and LMO thin-film depositions were performed using pulsed laser deposition to achieve low resistivity constituent materials for LSMO/LMO superlattice heterostructures on (100)-strontium titanate substrates. The schematic of the structure and the x-ray diffraction result are shown in Fig. 5. X-ray diffraction and high-resolution reciprocal space mapping indicate that the superlattices are epitaxial and pseudomorphic.

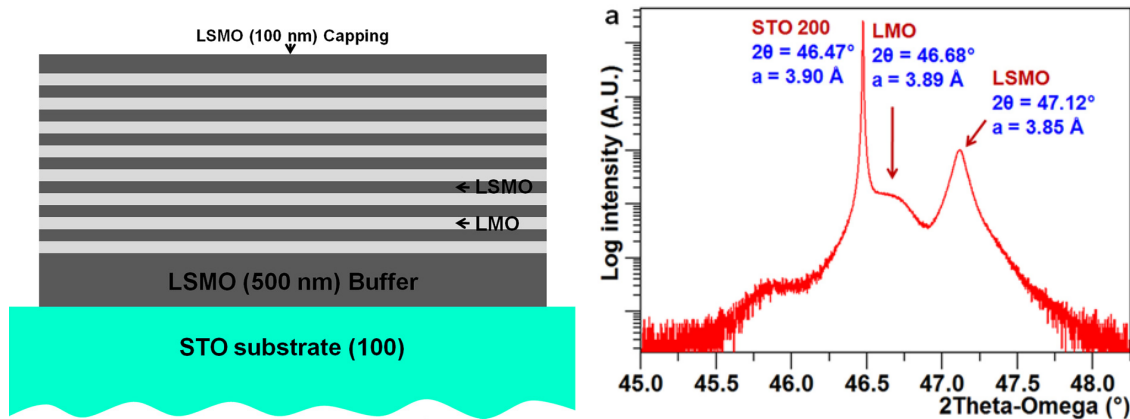


Figure 5. Schematic of metallic LSMO (8 nm)/semiconducting LMO (8 nm) superlattice (LSMO/LMO)₅₁ structure grown by PLD (left), and the x-ray diffraction 2-theta-omega scan of the superlattice (right).

Cross-plane devices were fabricated by etching cylindrical pillar structures in superlattices using inductively coupled plasma reactive-ion etching. The crossplane electrical conductivity data for LSMO/LMO superlattices reveal a lowering of the effective barrier height to 223 meV as well as an increase in cross-plane conductivity by an order of magnitude compared to high resistivity superlattices as shown in Fig. 6(a). These results suggest that controlling the oxygen deficiency in the constituent materials enables modification of the effective barrier height and increases the cross-plane conductivity in oxide superlattices.

The cross-plane LSMO/LMO superlattices showed a giant Seebeck coefficient of 2560 $\mu\text{V}/\text{K}$ at 300 K that increases to 16 640 $\mu\text{V}/\text{K}$ at 360 K as shown in Fig. 6(b). The giant increase in the Seebeck coefficient with temperature may include a collective contribution from the interplay of charge, spin current, and phonon drag. The low resistance oxide superlattices exhibited a room temperature cross-plane thermal conductivity of 0.92 $\text{W}/\text{m K}$, this indicating that the suppression of thermal conductivities due to the interfaces is preserved in both low and high resistivity superlattices. The high Seebeck coefficient, the order of magnitude improvement in cross-plane conductivity, and the low thermal conductivity in LSMO/LMO superlattices resulted in a two order of magnitude increase in cross-plane power factor and thermoelectric figure of merit (ZT), compared to the properties of superlattices with higher resistivity that were reported previously.

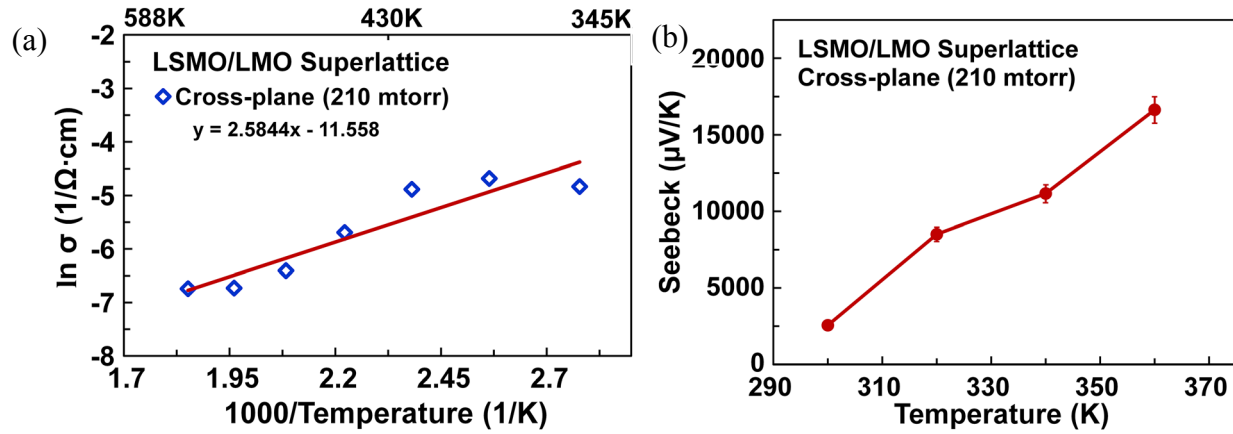


Figure 6. (a) Arrhenius plot of cross-plane LSMO/LMO superlattice electrical conductivity. The fitting extracted an effective barrier height of 223 611 meV. (b) The LSMO/LMO superlattice cross-plane Seebeck coefficient measurement using thermal imaging technique.

3. Epitaxial ScN films deposited by reactive magnetron sputtering (Purdue/UCSC)

Epitaxial ScN(001) thin films were grown on MgO(001) substrates by dc reactive magnetron sputtering. The deposition was performed in an Ar/N₂ atmosphere at 2×10^{-3} Torr at a substrate temperature of 850 °C in a high vacuum chamber with a base pressure of 10^{-8} Torr. Figure 7 is an FESEM plan-view image of a ScN film obtained using a high resolution through-lens backscattering electron detector.

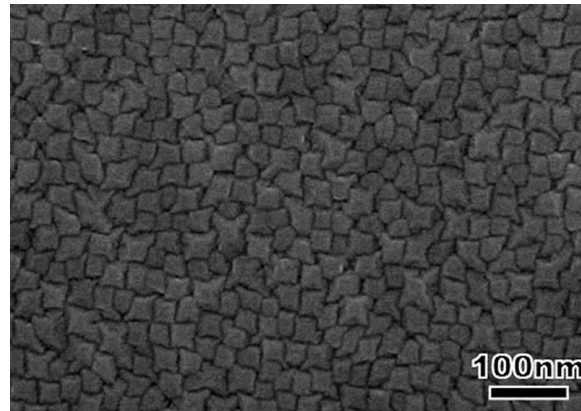


Figure 7. Plan-view FESEM image of the ScN surface showing the formation of square flat-topped mounds with average estimated feature size of 40 nm.

The square densely packed features with an average feature size of 40 nm are present on film surface. These features correspond to the formation of kinetically driven mound structures. Similar formations were previously observed in some semiconductors and transmission metal nitrides as well as in ScN single crystalline sputtered thin films. An Ehrlich-Schwoebel surface diffusion barrier

inhibits adatom migration down steps, thereby promoting nucleation on terraces and leading to the formation of mounds. As the film growth continues, mounds connect along the edges with the development of the cusps. Shadowing during further deposition and reduced adatom mobility at cusps leads to nanopipe formation along the mound edges and surface roughening. Thus, these features with four-fold symmetry, as expected for the nucleation of rocksalt ScN, represent the growth front of the ScN thinfilms. Nevertheless, the film surface is relatively smooth with a root mean square (RMS) surface roughness of 0.31 nm obtained from the AFM $2 \times 2 \mu\text{m}$ area scan.

In spite of oxygen contamination of 1.6 ± 1 at. %, the electrical resistivity, electron mobility, and carrier concentration obtained from a typical film grown under these conditions by room temperature Hall measurements are $0.22 \text{ m}\Omega\cdot\text{cm}$, $106 \text{ cm}^2 \text{ V}^{-1} \text{ s}^{-1}$, and $2.5 \times 10^{20} \text{ cm}^{-3}$, respectively. These films exhibit remarkable thermoelectric power factors of $3.3\text{--}3.5 \times 10^{-3} \text{ W/mK}^2$ in the temperature range of 600 K to 840 K as shown below in Fig. 8. The cross-plane thermal conductivity is 8.3 W/mK at 800 K yielding an estimated ZT of 0.3.

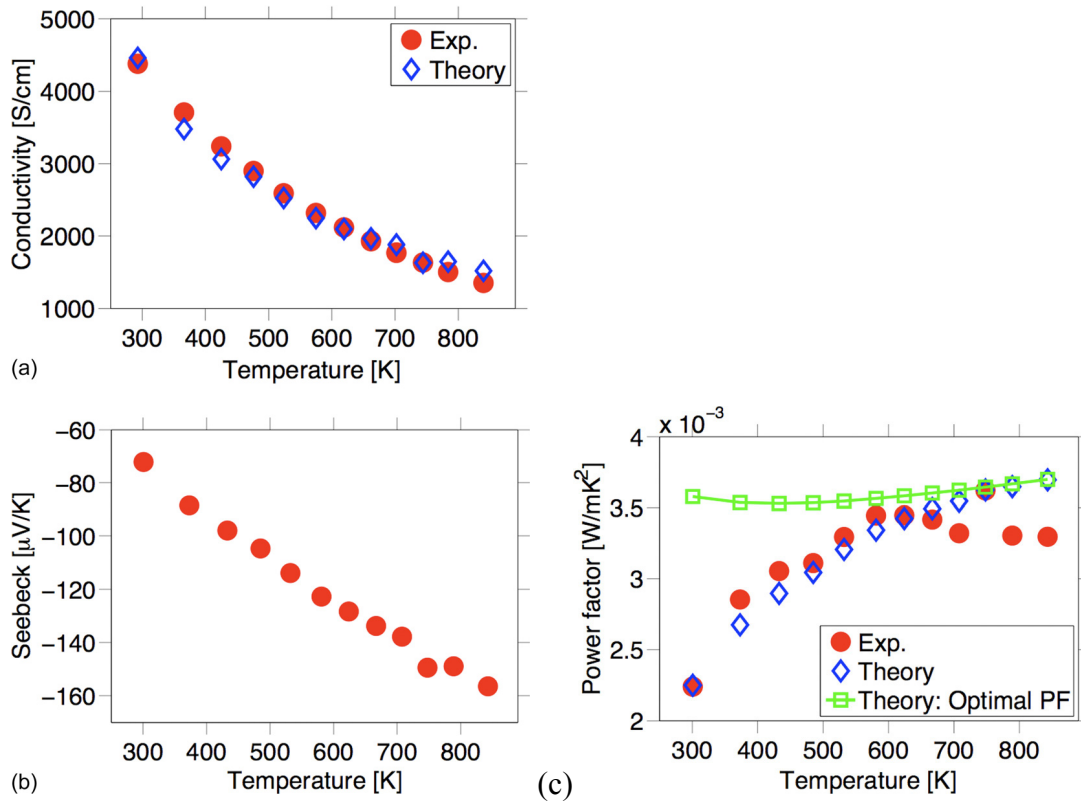


Figure 8. (a) In-plane electrical conductivity, (b) in-plane Seebeck coefficient, and (c) power factor of a ScN film measured under vacuum in the 300-840 K temperature range. The power factor increases with temperature reaching a maximum value of $3.5 \times 10^{-3} \text{ W/mK}^2$ at 600 K, which is in good agreement with the theoretical optimal power factor.

Theoretical modeling of the thermoelectric properties of ScN calculated using a mean-free-path of 23 nm at 300 K is in very good agreement with the experiment. Note that the theoretical Seebeck was set equal to the experimental Seebeck in order to determine the location of the Fermi level at each temperature. The extracted Fermi level was used to compute the electrical conductivity. The theoretical

power factor was calculated using a mean-free-path for backscattering of 23 nm at 300 K. The optimal power factor was obtained by varying the location of the Fermi level to maximize the power factor. These results also demonstrate that further optimization of the power factor of ScN is possible.

First-principles density functional theory combined with the site occupancy disorder technique was used to investigate the effect of oxygen contamination on the electronic structure and thermoelectric properties of ScN. The computational results suggest that oxygen atoms in ScN mix uniformly on the N site forming a homogeneous solid solution alloy. Behaving as an n-type donor, oxygen causes a shift of the Fermi level in ScN into the conduction band without altering the band structure and the density of states as shown in Fig. 9.

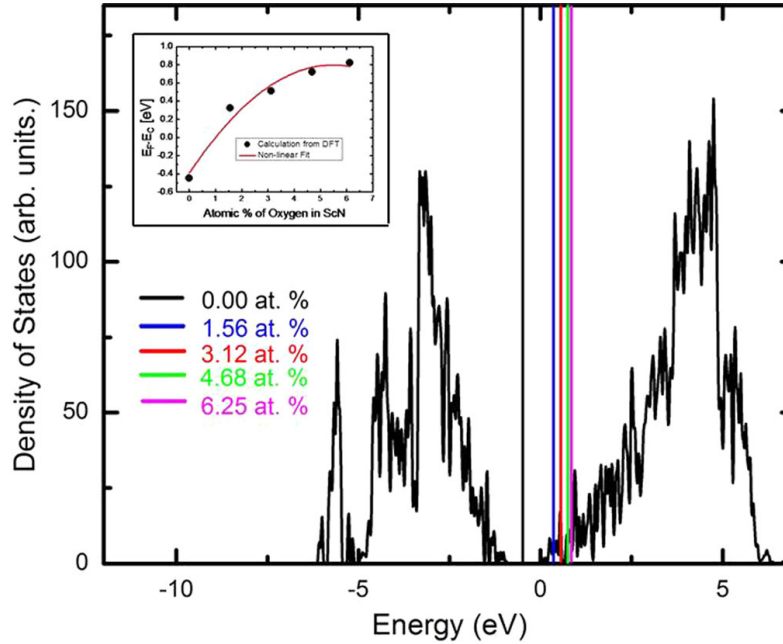


Figure 9. Calculated densities of electronic states as a function of the oxygen content in ScN films. The Fermi energy shifts in the conduction band as the concentration of oxygen is increased in ScN from 0.00 to 6.25 at. %, while the basic electronic band structure is preserved. Insert is the second-order polynomial fit of $(E_F - E_C)$ vs. oxygen concentration, which is used to estimate the position of the Fermi energy for oxygen content below 1.56 at. %.

4. Z-meter optimized for characterization of superlattice laminates (Purdue)

Through support of the DARPA grant a novel approach was developed for fabricating bulk-like laminate thermoelectric elements from nanostructured thin film superlattices (Figure 10).

The laminate process demonstrates the feasibility of fabricating bulk-like devices for real world applications and these bulk-like elements make it possible to simultaneously measure the thermoelectric properties (S , σ , and κ) of metal/semiconductor superlattices using a Z-meter, a custom characterization tool originally designed at MIT. Measuring the thermoelectric properties of the thermoelectric element provides a feedback loop for optimization of film parameters.

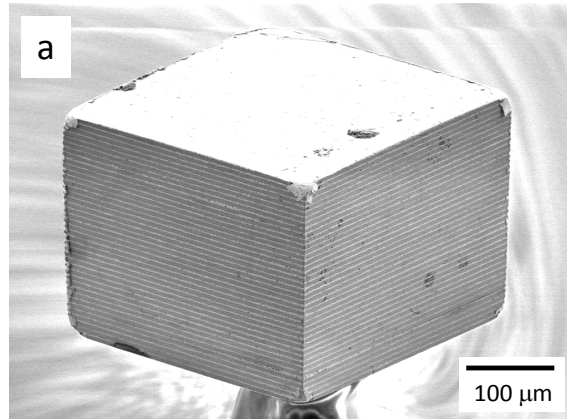


Figure 10. FESEM image of a polished 300 μm x 300 μm x 290 μm (Hf_{0.5}Zr_{0.5})N/ScN laminated thermoelectric element.

Initial measurements of laminate thermoelectric elements were conducted with a Z-meter at MIT. However, the MIT Z-meter was not able to go to very high temperatures with moderate temperature gradients. It therefore became critical that Purdue optimize this characterization technique to extract material properties which show the potential of metal/semiconductor multilayers.

5. TbAs:InGa(Al)As nanocomposites growth (Delaware)

In the past year, both the growth and characterization efforts at UD have made substantial progress. Specifically, we have grown TbAs:InGaAs and TbErAs:InGaAs materials, determined optimal TbAs concentrations over a wide temperature range, and successfully demonstrated significant increases in thermoelectric power factor (more than 80% increase vs. InGaAs) and ZT ($ZT \sim 1.1$) at moderate temperatures (up to 600K). Additionally, our understanding of TbAs and TbAs-containing materials has been advanced significantly, enabling further advances. On the characterization side, we have characterized the structure and composition (XRD and RBS) as well as the electronic transport properties (wide-temperature Hall effect and room-temperature Seebeck coefficient) of these materials, and through collaborations with UCSC, UCSB, and UC Berkeley, determined nanostructure (STEM), thermal conductivity (TDTR and 3ω), and moderate temperature thermoelectric properties (electrical conductivity and Seebeck coefficient from low temperature up to 600K).

The rationale behind TbAs-containing materials was based on the expected band alignment between TbAs and InGaAs. In previous work, ErAs:InGaAs thermoelectric materials (with ErAs composition $> 0.3\%$) did not show a significant increase in thermoelectric power factor because the ErAs nanoparticle pinned the Fermi level the near conduction band edge. Power factor was increased in ErAs:InGaAlAs materials, but the InGaAlAs matrix was not ideal due to its wider bandgap, larger effective mass, and lower mobility. By switching the rare-earth species from erbium to terbium, it was expected that the Fermi level would be pinned slightly lower, allowing energy-dependent carrier scattering without the inherent disadvantages of aluminum containing materials.

In previous years of the program, significant challenges consisted of developing of a highly-custom molecular beam epitaxy (MBE) system for the growth of rare-earth-V (RE-V)/III-V nanocomposites and determining the parameters required to grow terbium containing materials. Through these successes, significantly more rapid progress has occurred in the past year. Specifically, achievements within the past year include:

- Growth of TbAs:GaAs nanocomposites
 - Demonstration of high resistivity and short carrier lifetimes in these materials
 - Determination of relationship between TbAs content and lattice parameter through x-ray diffraction (XRD) and Rutherford Backscattering Spectrometry (RBS) study of materials with varying Tb content
 - Demonstration of nanoparticle formation (through both optical absorption and Scanning Transmission Electron Microscopy studies) with sizes of ~ 1 nm diameter
 - Characterization of band structure in TbAs nanoparticles (demonstrating probable presence of a bandgap within TbAs nanoparticles)
- Growth of TbAs:InGaAs nanocomposites
 - Determination of structure and presence of nanoparticles (including STEM)
 - Measurement of room-temperature (RT) thermoelectric properties (Hall effect, conductivity, Seebeck coefficient, and thermal conductivity) vs. TbAs content, showing an optimum RT performance in 0.3% TbAs samples ($ZT \sim 0.2$)
 - Determination of optimal moderate temperature (≤ 600 K) performance in $\sim 0.8\%$ TbAs samples, with $>80\%$ increase in power factor (significantly larger than any other material to date) and highly-promising $ZT \sim 1.1$ at 600 K.
 - Found lack of significant thermal conductivity reduction in TbAs:InGaAs (compared to ErAs:InGaAs), leading to theory (now being tested) that strain ($\sim 2.2\%$ in ErAs:InGaAs, $<0.9\%$ in TbAs:InGaAs) contributes significantly to phonon scattering
- Growth of TbErAs nanoparticles
 - Theorized that mixed-RE materials could allow both the large increases in power factor in TbAs:InGaAs and significant reductions in thermal conductivity observed in ErAs:InGaAs.
 - Grown a variety of concentrations of Tb and Er in TbErAs materials, which are currently being tested
- Hall effect characterization of project materials
 - We have measured the carrier concentration and mobility of a wide variety of project materials (from UD, Purdue, and UCSB) over a wide temperature range (20-800 K) to aid understanding of project materials.

6. Nitride Metal/Semiconductor Superlattices (Purdue)

A. Scandium nitride optimization for nitride metal-semiconductor superlattices

Hall effect measurements of the original scandium nitride (ScN) thin-films showed carrier concentrations of $7 \cdot 10^{20}$ - $2 \cdot 10^{21}$ cm^{-3} with low mobility values of 0.6 - 2.5 $\text{cm}^2/\text{V}\cdot\text{s}$. Ideally, the carrier

concentration should be $< 10^{19} \text{ cm}^{-3}$. Various causes have contributed to these less than ideal electrical properties. First, it was discovered that multiple scandium targets were contaminated with tungsten (2.7 – 3.7 atomic %). New tungsten-free scandium targets led to an increased mobility ($25 \text{ cm}^2/\text{V-s}$) in the as-deposited ScN thin films, but no significant reductions in the carrier concentration ($3 \cdot 10^{20} - 2 \cdot 10^{21} \text{ cm}^{-3}$). Subsequent x-ray photoelectron spectroscopy (XPS) results revealed the presence of high-levels of oxygen contamination (4 - 20 atomic % depending on growth parameters) in the ScN thin-films, with oxygen acting as a donor. The high levels of oxygen lead to highly degenerate ScN films with carrier concentrations in the 10^{20} - 10^{21} cm^{-3} range and a lower than desirable electron mobility.

Purifiers were installed on the nitrogen and argon process gas lines of the nitride sputter deposition system to eliminate any potential oxygen source from these process gases. The purifiers did not alter the oxygen levels detected in the ScN thin films, which leads us to believe that the oxygen source is residual water vapor. Internal IR bake-out lamps and a liquid nitrogen cold-trap are currently being reviewed as candidates for reducing residual water vapor in the chamber. Correlations between the ScN microstructure (TEM imaging) and oxygen concentrations of thin films grown under a variety of deposition conditions indicate that post-growth oxidation is potentially occurring along grain boundaries. The fact that the measured carrier concentration (Hall effect) does not track with the oxygen concentration supports the hypothesis of grain boundary oxidation. Additional ScN samples with in-situ nickel diffusion barriers (capping layer) are currently being characterized by glow discharge spectroscopy to determine whether oxidation is dominant during growth or post-growth. Reducing or eliminating oxygen from the ScN thin films is critical for optimizing the carrier concentration and electron mobility, thus explaining the reason for continued focus in this area.

B. Contact resistivity of nitride metal-semiconductor superlattices

Electrical characterization of the nitride metal-semiconductor superlattices requires contacts with extremely low contact resistivity (e.g. 10^{-8} Ohm-cm^2). In addition, low contact resistivity values are necessary for reduced parasitics in bulk-like laminate structures. Fortunately, the nitride metal-semiconductor superlattice structures end with a metallic nitride (e.g. HfN or ZrN), which allows a low resistivity metal-metal contact to be fabricated. However, Cr-Au and Ti-Au contacts on metallic nitrides initially showed unsuitably high contact resistivity values (e.g. 10^{-3} Ohm-cm^2), presumably due to surface oxidation. Further research revealed that a simple surface treatment of the metallic nitride in buffered oxide etch (BOE) prior to contact deposition lowered the contact resistivity to less than 10^{-7} Ohm-cm^2 . IVT measurements corroborate these results. The resistance values of the IVT pillar device structures indicate a contact resistivity $< 5 \cdot 10^{-8} \text{ Ohm-cm}^2$, which shows that the metal-metal contacts are initially of excellent quality. Preliminary contact annealing studies indicate that repeated temperature cycling does not significantly alter the contact properties. However, issues with the IVT measurements that are used for barrier height characterization indicate that a diffusion barrier between the chromium/titanium and gold may be required to ensure stable contacts at elevated temperatures. Devices are currently being fabricated with Pt diffusion barriers for further IVT characterization.

C. IVT characterization of nitride metal-semiconductor superlattices

Nitride metal-semiconductor superlattices of varying composition and period have been sputter deposited and fabricated into pillar device structures using focused ion beam (FIB) milling. Please refer to the summary from the University of California, Santa Cruz for detailed IVT analysis of these

samples. To summarize, IVT results have so far shown thermionic behavior in ZrN (4nm)/ScN (12nm) superlattices with calculated barrier heights consistent with previously deposited ZrN/ScN superlattices. Additional ZrN/ScN superlattices with constant ZrN thickness (4 nm) and varying ScN thickness (i.e. 4, 8, 20, and 50 nm) have been deposited, but IVT results only show metallic behavior. The cause of the inconsistent IVT measurements is still being investigated, with likely causes being residual damage from the FIB process or contact degradation. HfN/ScN superlattices have only exhibited metallic behavior, indicating a negligible or non-existent Schottky barrier height.

As discussed in the previous section, IVT results indicate that the contacts have an initial contact resistivity $< 5 \cdot 10^{-8}$ Ohm-cm². However, repeated temperature cycling of the thermionic behaving ZrN/ScN superlattice shows that the superlattice reverts back to metallic behavior after multiple temperature cycles. These results indicate potential contact degradation, but the contact annealing studies contradict this hypothesis. To sort out this contradiction, research on the effect of temperature cycling on contact integrity is currently ongoing.

7. Bulk Growth of (Ga,In)As and (Ga,In)Sb with Erbium nanoprecipitates (Purdue)

Bulk ingots of (Ga_{0.8}In_{0.2})Sb with varying erbium concentrations (0.5%, 1%, 2%, and 3%) and (Ga_{1-x}In_x)As with varying indium concentrations (x=0.1, 0.2, 0.3, and 0.5) and varying erbium concentrations (1%, 2%, and 3%) were grown and characterized. The overall indium concentration measured with EDS was much lower than expected (e.g. 1% indium present in 10% nominal indium) and the indium exhibited a non-uniform spatial distribution. The microstructure was composed of grains with widely varying indium concentrations and the erbium was present in large grains (i.e. ~100 μ m) of ErSb and ErAs instead of forming nanoprecipitates. Due to growth difficulties, the bulk growth project was defunded to maintain focus on the nitride metal-semiconductor superlattices.

8. MOCVD growth (UCSC)

With the support of DARPA/DSO, we have been conducting two development activities; *Equipment Development* and *Thermoelectric Materials Development* by metal organic chemical vapor deposition (MOCVD) in collaboration with Structured Materials Industries, Inc. (Piscataway, NJ). One graduate student researcher (Takehiro Onishi/UCSC, 50%) and one engineer (Elane Coleman, SMI Inc., 5%) have been supported by this program. The focus has been to develop Zn-doped InGaSb and InSbAs ternary alloys that contain ErSb nanostructures by MOCVD. The MOCVD efforts are viewed as a complementary approach to those conducted with molecular beam epitaxy within this program. We have also devoted ourselves developing InGaAs ternary alloys that contain ErAs nanoparticles because of InGaAs being lattice-matched to semi-insulating InP substrates simplifying the extraction of thermoelectric properties and clarifying advantages offered by employing MOCVD for this program. The following sections describe the progress of the MOCVD efforts (Please note the MOCVD efforts have been ceased as of February 3, 2011 due to the realignment of the program).

A. Reflection Absorption InfraRed Spectroscopy (RAIRS)

Since over all physical properties of nanocomposites (i.e., ErSb/InGaSb and ErSb/InSbAs) depend critically on the size and volume density of semi-metallic nanoparticles, accurate and precise control on the delivery of an Er precursor and assessment on the incorporation of Er on InSb surfaces are imperative. Unlike molecular beam epitaxy, in-situ growth monitoring systems capable of characterizing and estimating

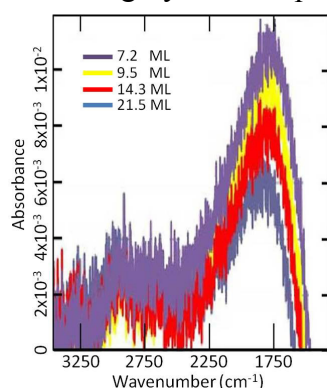


Fig. 12: RAIRS spectra collected from the samples with various amounts of ErSb.

the presence of a small amount of materials on a growing surface are not generally available in MOCVD therefore; we explored an ex-situ calibration technique, RAIRS, to collect information on vibrational modes of In-H bonds existing on InSb surfaces and to calibrate a small amount of ErSb delivered onto InSb surfaces during MOCVD growth runs.

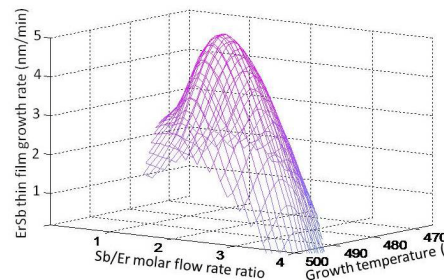


Fig. 11: The deposition rate of ErSb thin films on InSb(100) surfaces.

Fig. 11 shows the dependence of the growth rate of ErSb thin films on two growth parameters; growth temperature and Sb/Er molar flow rate ratio. Apparently, the growth rate of ErSb is extremely sensitive to these two growth parameters, clearly suggesting the need for an ex-situ

calibration technique with sensitivity of few ErSb monolayers.

Fig. 12 shows RAIRS spectra obtained from four ErSb samples with different amounts of ErSb (7.2 to 21.5 monolayers) deposited on InSb surfaces. It is apparent that as the amount of deposited ErSb increases (i.e., InSb surface area decreases), the RAIRS absorption peaks associated with the In-H bonds ($\sim 1740 \text{ cm}^{-1}$) decreases. Also notable in Fig. 4 is the capability of RAIRS to distinguish a 2.3 ML difference in the ErSb amount. To further assess the small amount of ErSb deposition profiled by RAIRS, we also investigated surface morphology of the two samples representing 7.2 ML and 21.5 ML by atomic force microscope (AFM) as shown in Fig. 13(a) and (b), respectively. Clearly seen are ErSb islands covering the surface of InSb buffer layers. On the 7.2 ML sample in (a), the InSb surface is approximately 65.3% covered and on the 21.5 ML sample in (b), the InSb surface is approximately 81.5% covered. These AFM results are consistent with the RAIRS results and further qualify RAIRS as a competent ex-situ calibration technique for evaluating the deposition of few to tens of mono-layer amounts of ErSb on In-H terminated InSb surfaces.

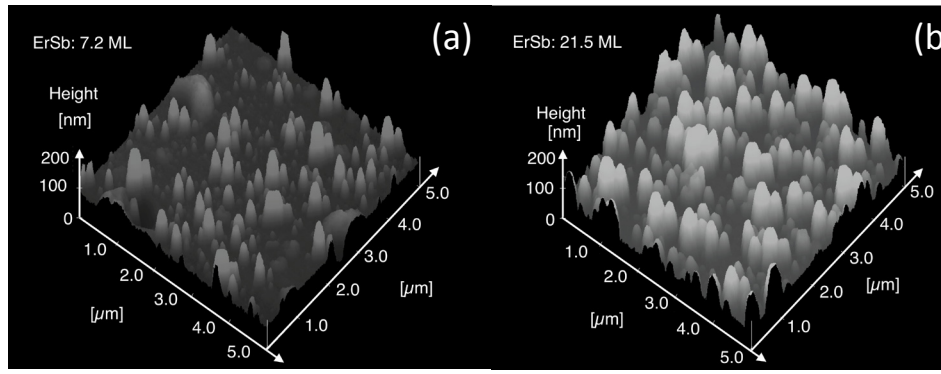


Fig. 13: AFM images of (a) 7.2ML ErSb and (b) 21.5 ML ErSb deposited on InSb(100) surfaces.

B. Thermal conductivity of ErSb/InGaSb:Zn and ErSb/InSbAs:Zn nanocomposites

Using MOCVD, we grew two types of nanocomposites, Zn-doped ErSb/InGaSb and Zn-doped ErSb/InSbAs. Cross-sectional transmission electron microscope (XTEM) images obtained from ErSb/In_{1-x}Ga_xSb:Zn ($x=0.97$) and ErSb/InSb_{1-y}As_y:Zn ($y=0.41$) nanocomposites are shown in Fig. 14(a) and (b), respectively. The XTEM images were collected along [110] zone-axis.

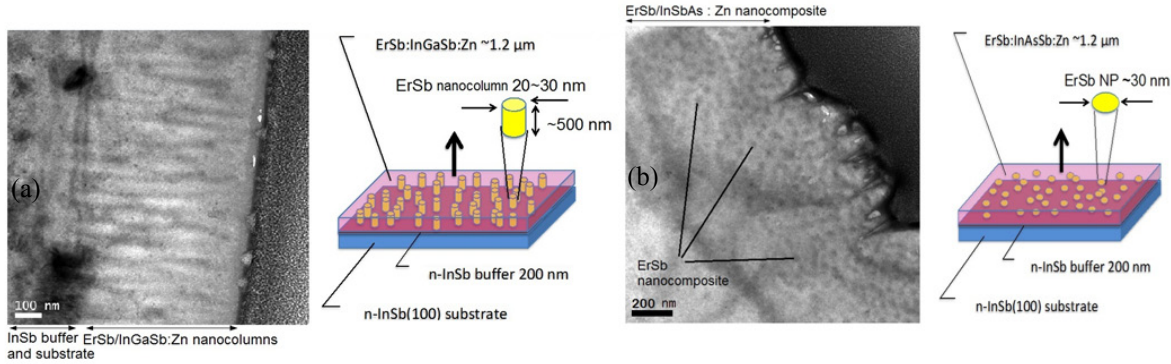


Fig. 14: XTEM image of (a) Zn-doped ErSb/InGaSb nanocomposite and (b) Zn-doped ErSb/InSbAs nanocomposite.

Fig. 14(a) reveals that a group of 20-30 nm diameter ErSb nanocolumns formed in the InGaSb:Zn host while Fig. 6(b) shows a large number of ~30 nm diameter ErSb nanoparticles formed in the InSbAs:Zn host. We further utilized time domain thermo-reflectance (TDTR) to determine thermal conductivity of another set of nanocomposites at room temperature (Prof. Ali Shakouri's group/UCSC). The thermal conductivity obtained for ErSb/InSb_{1-y}As_y:Zn ($y=0.41$) nanocomposite is 4.0 ± 0.6 W/mK, which is slightly lower than the alloy limit. The thermal conductivity of ErSb/In_{1-x}Ga_xSb:Zn ($x=0.35$) nanocomposite is found to be 7.1 ± 0.7 W/mK, which is slightly higher than the alloy limit.

C. Extended X-ray Absorption Fine Structure (EXAFS)

EXAFS data were collected at the Er L3 edge at the Stanford Synchrotron (Prof. Frank Bridges' group/UCSC) for a range of samples in which ErSb nanoparticles were embedded in either GaSb or InGaSb host with Er concentrations in the range from 0.5% to 10% (The samples were grown by Prof. Art Gossard's group/UCSB). EXAFS probes the local structure of the Er atoms in the samples. The data for two thin films (thickness 2 μm and 100 nm) of pure ErSb are shown in Fig. 15(a) as a reference. The first peak is for Er-Sb and appears to be a double peak (with maxima at 2.3 and 2.9 \AA) but is only a result of energy dependent backscattering amplitude. The next peak is Er-Er at 4.1 \AA in Fig. 15(a). Fig. 15(b) shows corresponding Er L3 edge results for ErSb/GaSb with 0.5 and 10% Er. Note that the shape of both peaks is very similar to the pure ErSb reference in Fig. 7(a). Fig. 15(c) shows that the results for 0.8% Er in two types of ErSb/ $\text{In}_x\text{Ga}_{1-x}\text{Sb}$ hosts ($x=0.7$ and $x=0.5$) are similar.

A detailed EXAFS analysis was performed on all samples. Based on the EXAFS analysis the first and second neighbor peaks (Er-Sb and Er-Er peaks) of all samples roughly resemble the pure ErSb reference results. Replacing most of the Er atoms with Ga or In atoms at the same lattice locations did not improve the fit, suggesting that the second neighbors about the Er atoms are primarily Er; and there is no evidence for a significant fraction of Ga or In second neighbors. The Er-Er second peak at approximately 4.0 \AA was slightly reduced for the $\text{In}_x\text{Ga}_{1-x}\text{As}$ ($x=0.5$) sample in Fig. 15(c). For this sample, there may be smaller ErSb nanoparticles for which nanoparticle surface effects become important, or there is more disorder in the crystal structure. We conclude that ErSb nanoparticles have atomically sharp boundaries in both GaSb and InGaSb hosts for concentrations in the range of 0.05-10%. The varying amplitude of the Er-Er peak may indicate the presence of nanoparticles with different sizes or more disorder. More detailed measurements would be needed to estimate the nanoparticle sizes. Our results show that EXAFS is a useful technique for determining the local structure around dilute atoms such as Er and can verify whether clustering has occurred.

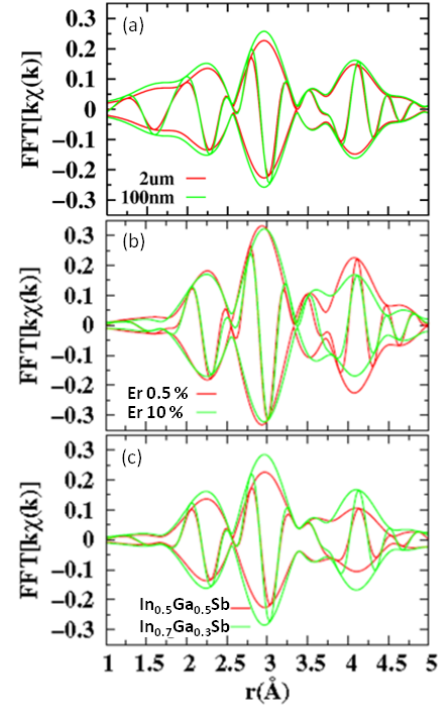


Fig. 15: EXAFS of ErSb/GaSb and ErSb/InGaSb nanocomposites.

9. High temperature characterization (UCSC, UCSB)

A. Substrate transfer for high temperature measurements

Oxide-to-oxide bonding is desired for the substrate transfer for high temperature electrical measurements. PECVD (Plasma-Enhanced Chemical Vapor Deposition) SiO_2 is highly insulating and stable at very high temperatures so that it is commonly used for high temperature insulation and surface encapsulation. The reactive hydrophilic surface and structural porosity of SiO_2 layers make the oxide a good bonding interface layer as well, and even lower the required temperature for strong covalent bonding. We performed the oxide bonding for this substrate transfer task (see Figure 16 for process flow). The bonding was annealed at 300°C for two hours to increase the bond strength. This

annealing temperature is quite low compared to those of other conventional bonding techniques, which are often as high as 1000. Lowering the bonding temperature is very important because strain induced by the thermal expansion mismatch between the two bonded substrates can degrade the material quality and change the properties of the materials involved. Our strain analysis indicates that less than 5% of electrical conductivity at 800 K is altered by the additional strain from the oxide bonding.

For high yield from the bonding process, ultra low surface roughness is required. The surface roughness of the commercial Sapphire wafer used in the bonding process was as low as 5 Å, and the 30 nm thick PECVD SiO₂ that was used as a bonding interface layer had peak-to-peak roughness less than 10 Å, which is in a suitable range for bonding. However, the III-V InGaAlAs epitaxial layer grown by MBE had surface oval defects which were as tall as 2 μm from the epitaxial surface. In order to remove those defects from the film, a photolithography process was performed to make a 20~30 μm in diameter open hole of photoresist around each oval defect. Then the sample was dipped in H₃PO₄:H₂O₂:H₂O=1:5:15 to etch the open area down to the substrate and remove the oval defects. In the microscopic view of the bonded surface in Fig. 9 (left), one can see open holes in the thin film where the oval defects were removed by wet-etching. A square cloverleaf shaped van der Pauw (vdP) pattern with large contact areas on the four corners is fabricated on the 2 μm epitaxial layer by reactive ion etching (RIE) with Cl₂ gas as shown in step 5 in Fig. 16, after which surface passivation and metallization are performed (Fig. 17 right).

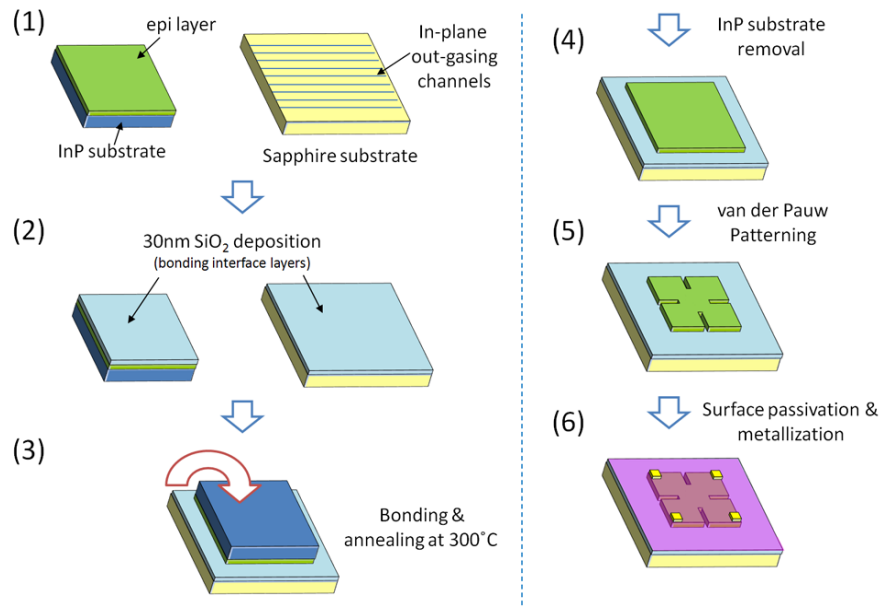


Fig. 16 Substrate transfer processing steps.

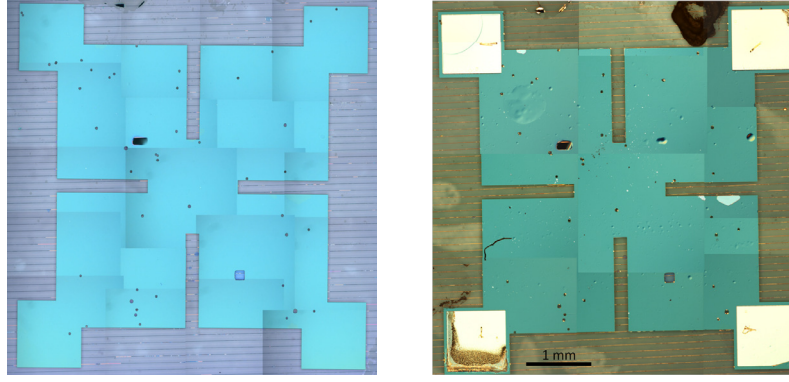


Fig. 17: (left) The bonded surface after the substrate wet etching and patterning of 0.5% ErAs:InGaAs. The total size of the bonded thin film area is $5.5 \times 5.5 \text{ mm}^2$; (right) A picture of the final substrate-transferred sample after a series of high temperature measurements up to 850 K.

A measurement has been done on 0.2% ErAs:InGaAs. The results of electrical conductivity is shown in Fig. 18. It can be seen that at high temperatures substrate conduction and backside silver paste leakage dominate in the sample without substrate transfer. It is necessary to transfer the film to non-conducting substrate for accurate high temperature measurements.

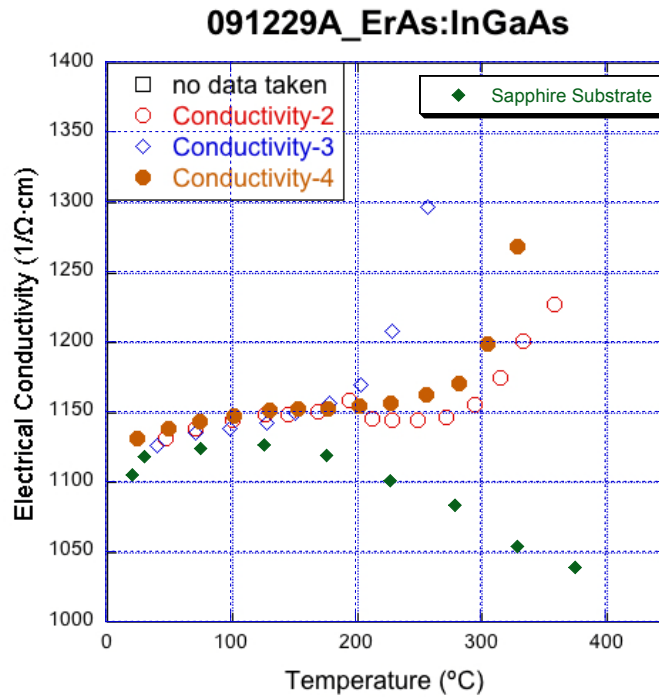


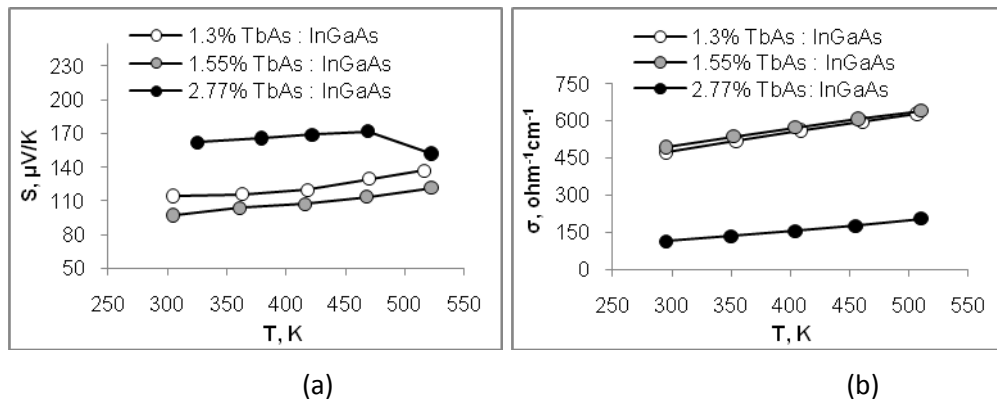
Fig. 18: Electrical conductivity of ErAs:InGaAs.

B. Characterization of InGaAs thin films embedded with rare earth nanoparticles

UCSB group developed an accurate and repeatable method for measurement of the Seebeck coefficient using an epitaxial reference. Steps for improving repeatability of high-temperature measurements was necessitated by a recent review article by the National Institute of Standard Technologies in the Journal of Applied Physics. (J. Martin *et al.*, “High-Temperature Seebeck Coefficient Metrology”, *J. Appl. Phys.*, Vol. 108, 121101, 2010)

UCSB group also characterized Terbium-doped InGaAs grown by the Zide group, University of Delaware, and demonstrated a record power factor of $4.16 \times 10^{-3} \text{ W/m-K}^2$ at 550 K on this material system using a new high-temperature (1000 °C maximum) vacuum chamber purchased under DARPA funding. We are also currently investigating a large discrepancy in Hall Effect measurements before and after standard wet chemical processing of Terbium doped InGaAs. Although the samples with highest power factors were relatively low doped and therefore did not suffer from this issue, the high doping regime is also worthy of characterization due to the promise of low thermal conductivity, and the source of these discrepancies needs to be investigated before reliable measurements can be reported on high (> 3%) Terbium-doped InGaAs.

Thermoelectric transport properties of InGaAs with high concentration of semimetallic TbAs embedded nanoparticles were studied in 300-600K temperature range at UCSC. Nanoparticle concentration studied were over 1%, in a regime where coherent multiple scattering could affect electron transport. Scattering by ionized embedded nanoparticles which are approximately one nanometer in diameter is significantly different from the standard ionized impurity doping. The Seebeck coefficient and electrical conductivity were characterized as a function of temperature. The occurrence of the energy dependent electron scattering was experimentally observed. The Seebeck coefficients were higher than that of pure InGaAs alloy at the same doping level for all the compositions considered. The electrical conductivity increased for the compositions with 1.3% and 1.55% of TbAs nanoparticles leading to over threefold thermoelectric power factor enhancement in the nanocomposite with 1.3% of Tb content. The measured room temperature thermal conductivity of TbAs:InGaAs nanocomposites was lower than that of pure InGaAs alloy resulting in further optimization of the thermoelectric performance. For these high terbium content samples, the maximum $ZT = 0.3$ was obtained at 500K for the composition with 1.3% Tb content. The measurement results are shown in Fig. 19.



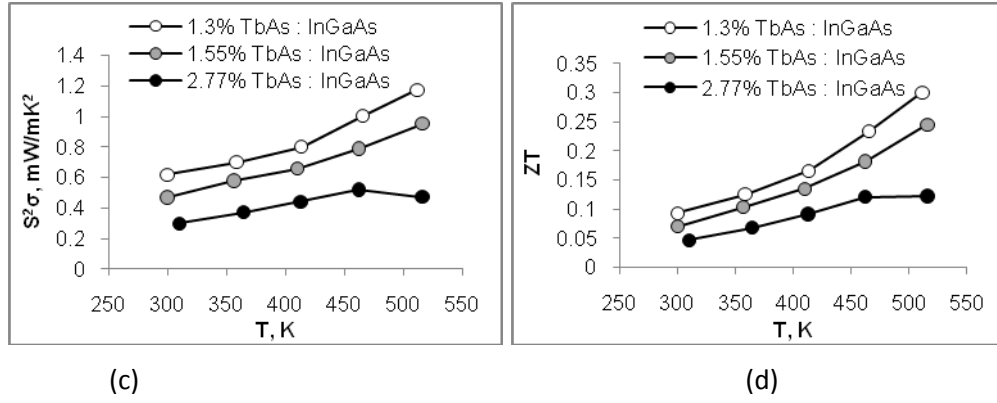


Fig. 19: (a) Seebeck coefficient, (b) electrical conductivity, (c) power factor, and (d) ZT, of high Tb concentration TbAs:InGaAs.

We also observed interesting anisotropic thermoelectric properties in the sample with 2.77% Tb content. It was found that it was 33% more resistive in one direction. The results are summarized in Fig. 20. We believe that this anisotropy is connected with the diffusion of the nanoparticles during the growth. The nanoparticles tend to diffuse along the fast diffusion direction (most probably along (110)). As the result the potential barriers are formed, which would affect the electronic transport across them. The measured Seebeck coefficient across the barriers (along the more resistive direction) was lower. However, as the temperature increased, the electron energy became enough to overcome the barriers and the thermopower approached the value measured in the direction along the barriers.

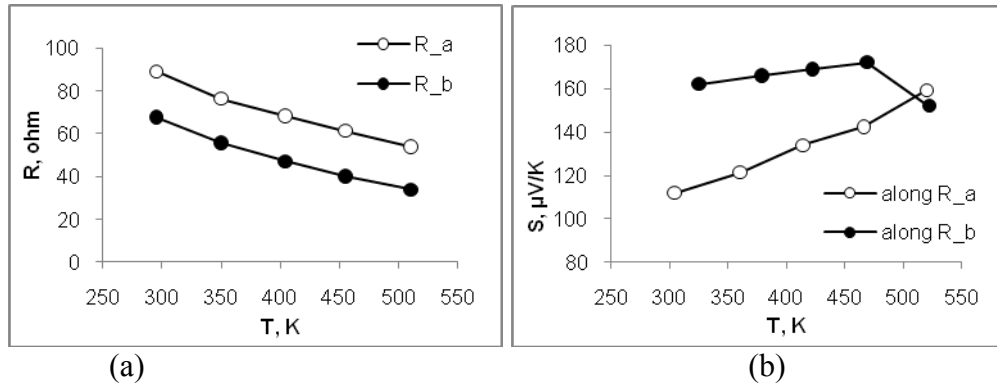


Fig. 20: Electrical resistance (a) and the Seebeck coefficient (b) measured in perpendicular directions in TbAs:InGaAs nanocomposite with 2.77% of Tb content.

C. Characterization of p-type ErSb:InGaSb

UCSC and UCSB groups performed electrical conductivity and Seebeck measurements on p-type ErSb:InGaSb. As can be seen in Fig. 21, very good agreements between UCSC data and UCSB data have been obtained.

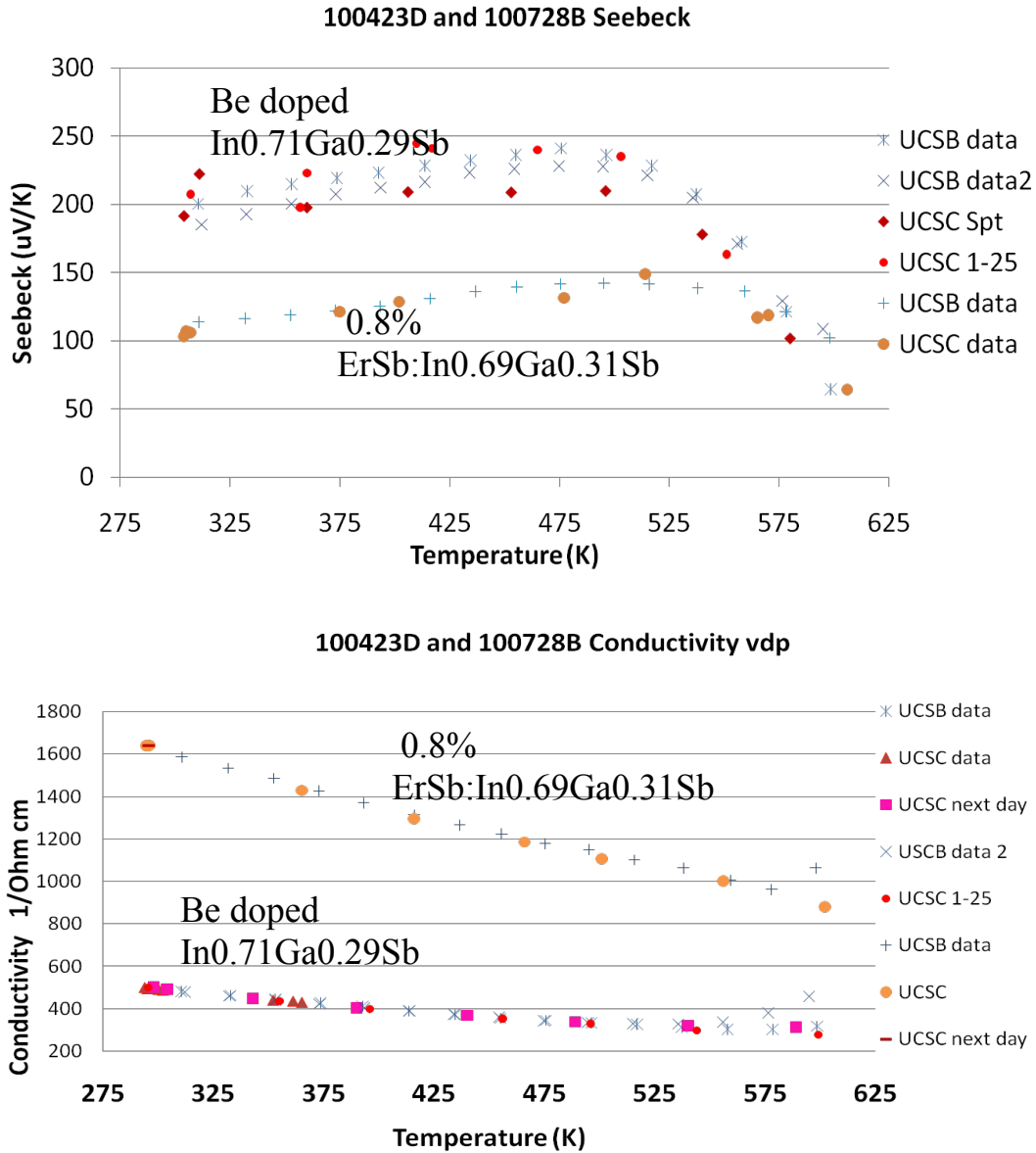


Fig. 21: Seebeck and Electrical conductivity of p-type InGaSb and ErSb:InGaSb.

D. Characterization of ZrN/ScN superlattices grown at Purdue

UCSC group have optimized the UCSC cryostat system for measuring IVT curves for electrical conductivity. We have modified the chamber to measure two devices on a sample simultaneously. We have also totally automated the measurement software so the experiment does thorough analysis that can take place overnight.

We observed thermionic trends in resistance versus temperature curves of the nitride superlattices. Specifically, we have only observed it consistently in ZrN/ScN superlattices with a period of 4nm/12nm at a thickness of 1um. Other periods and thicknesses have not shown repeatable trends as of yet. However, each cycle through high temperature measurements (up to 650 K) has had slightly

changing behavior. In the Conductivity versus Temperature data shown in Fig. 22, it shows that in the first day of measurement, the thermionic behavior is weak. On the second day, the thermionic trend is very strong, for a time, reaches a plateau, and then continues upward again. On the third day, the first thermionic trend does not appear, but there is an increase corresponding with the second trend of the second day. Our best explanation for this behavior is that there are multiple superlattice barriers in the material, corresponding the σ_2 and σ_3 . σ_1 corresponds to an electrical shunt that dominates at the lower temperatures. After each high temperature cycle, the electrical shunt seems to dominate more.

We have performed thermoreflectance imaging to observe Seebeck improvement with temperature. Thermoreflectance takes advantage of the small change in material reflectivity with temperature. By looking at the change in temperature as a function of current, we can determine the Seebeck coefficient of the material, and then we can heat the sample to get the Seebeck coefficient as a function of temperature, as shown in the Fig. 23. We see a substantial improvement of Seebeck coefficient as temperature increases. Further tests will be done with more temperature steps to get a more accurate picture of the Seebeck coefficient's behavior as temperature increases. Unfortunately, the thermoreflectance system is not in vacuum, so the temperature we can measure up to is limited. If we go beyond 450 K, the sample will begin to degrade outside of vacuum due to oxidation. We plan to put the samples in vacuum during future measurements.

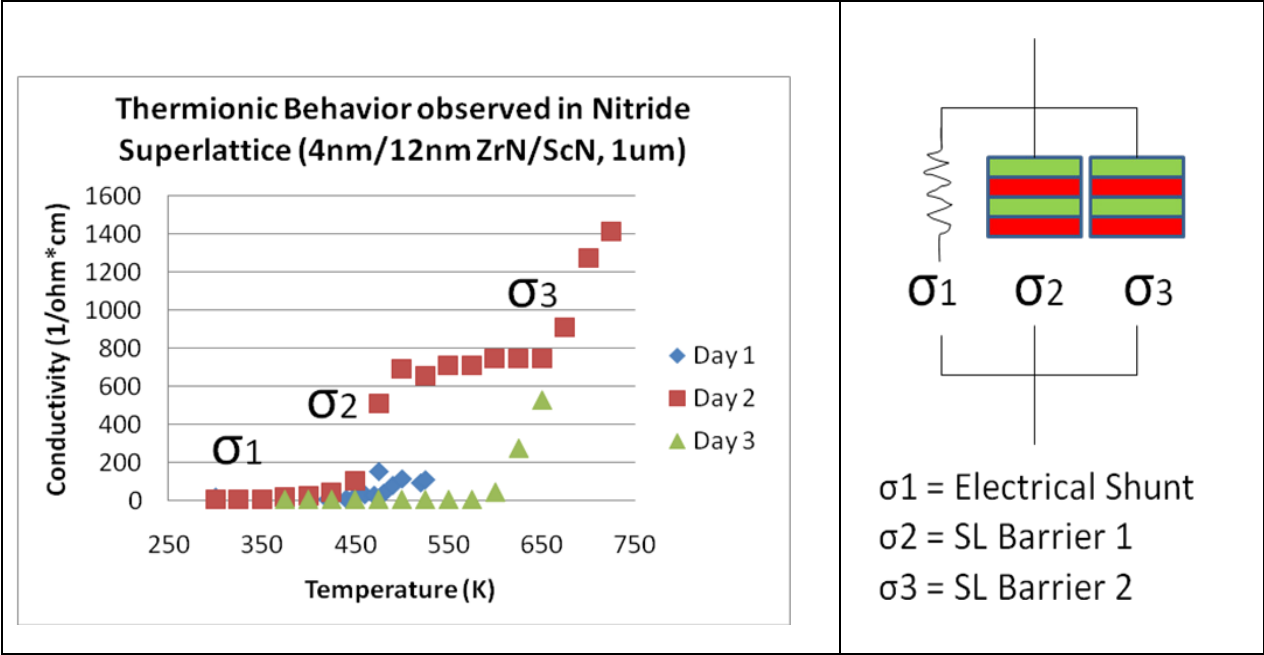


Fig. 22: Temperature dependence of electrical conductivity for ZrN/ScN superlattices and electrical network model.

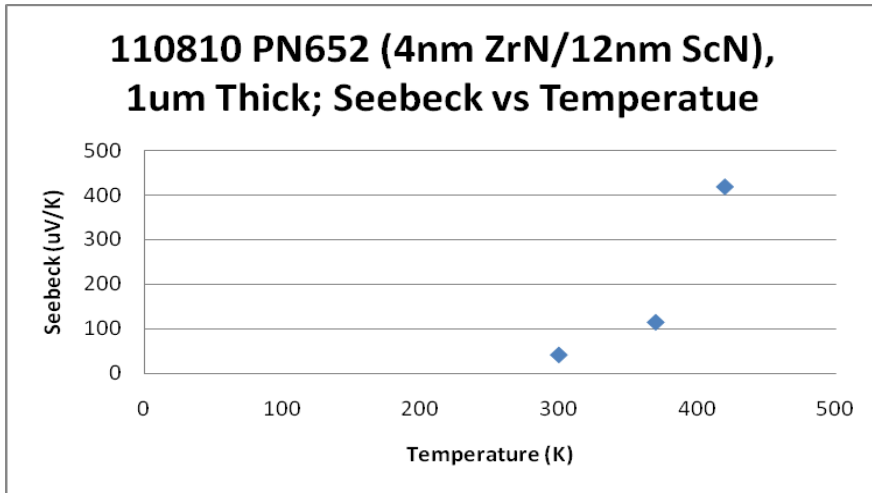


Fig. 23: Seebeck coefficient of ZrN/ScN superlattices as a function of temperature.

10. Thermal conductivity measurements and models (Berkeley)

Metal/semiconductor nanocomposites are promising material systems in the aspects of thermopower enhancement due to phenomena such as energy dependent charge carrier filtering, and thermal conductivity reduction by phonon scattering across interfaces or at nanoparticles. Especially, our previous study successfully demonstrated that the alloy limit could be beaten by embedded nanoparticles, which scatter mid to long-wavelength phonons in addition to alloy scattering. At UC Berkeley, the three-omega method was used to characterize the thermal properties of molecular beam epitaxially grown metal-semiconductor nanocomposites, which corresponds to newly given tasks in the past year, for a temperature range from 40K to 800K.

To summarize, in the past year, we have progressed in the following areas:

- 1) Thermal characterization of rare (Erbium) earth-doped InGaSb alloys: We have measured the thermal conductivity of numerous InGaSb films with different Indium contents
- 2) Thermal characterization of rare earth (Terbium)-doped InGaAs alloys: We have measured the thermal conductivity of numerous InGaAs films with different TbAs concentrations.
- 3) Thermal characterization of HfN:ScN superlattices: We have measured the thermal conductivity as a function of superlattice spacing.

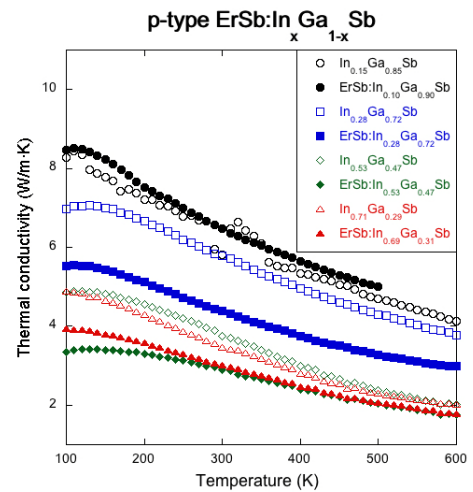


Figure 24. Temperature dependent thermal conductivity measurement on a series of $\text{In}_x\text{Ga}_{1-x}\text{Sb}$ samples with different In compositions and either doped with or without ErSb.

A. Thermal characterization of Erbium (Er)-doped InGaSb:

Inspired by the impressive results from Er-doped InGaAs, the p-type analog of Erbium doped InGaSb is considered as a promising candidate for solid state energy conversion. An initial trial was performed with Er-doped GaSb which has superior hole-mobility. Regarding the thermal property of this material, most of the heat is carried by short wavelength phonons so that significant reduction of thermal conductivity is not possible. Therefore, in order to scatter the short wavelength phonons efficiently, Indium was introduced and the Indium content (x) of $\text{In}_x\text{Ga}_{1-x}\text{Sb}$ was gradually increased to $x=0.7$ to find the optimum value. As predicted, the samples with higher Indium contents show lower thermal conductivity values.

Figure 25 shows simulation results based on the Boltzmann transport theory considering various scattering rates such as normal, Umklapp, alloy and nanoparticles. The alloy scattering rate (τ_{alloy}^{-1}) is expressed as

$$\tau_{\text{alloy}}^{-1} \propto x(1-x)\omega^4,$$

where x and ω are alloy composition and phonon angular frequency, respectively. Thus, relatively lower thermal conductivity near $x=0.5$ is explained by the above relation. Additionally, because short wavelength phonons play an important role in heat transport, the optimum size of embedded nanoparticles, which minimizes thermal conductivity, becomes relatively smaller to be about 2 nm. However, thermal conductivity changes less along the diameter direction, which indicates weak scattering by nanoparticles as shown in Figure 25.

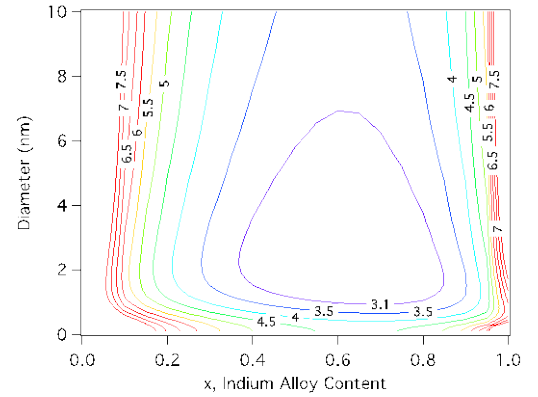


Figure 25 Contour Plot of Thermal Conductivity for ErSb:InGaSb as a function of particle size and Indium content (fixed 1% vol ErSb)

B. Thermal characterization of Terbium (Tb) doped InGaAs alloys:

The studies for the thermal characterization of Er-doped III-V materials have been reported previously, which attracted much attention due to the advantages of Er, such as electron donation and thermal conductivity reduction. Similar to its counterpart of Er, Tb is expected to donate electrons to an embedding matrix in the same way. Moreover, by virtue of a larger lattice constant of Tb compared to Er, the Fermi level of TbAs:InGaAs will be pinned near the conduction band edge resulting in an improvement in the power factor. TbAs:InGaAs samples with different TbAs concentrations of 0, 0.3, 0.8 and 1.55% have been measured. Based on the TEM images provided by the growers, no nanoparticle was found in the 0.3% TbAs sample, possibly due to high solubility of TbAs in InGaAs. On the other hand, nanoparticles with a ~ 1 nm diameter were observed in the 0.8% TbAs sample. Except for the 1.55% TbAs sample, as shown in Figure 26, the

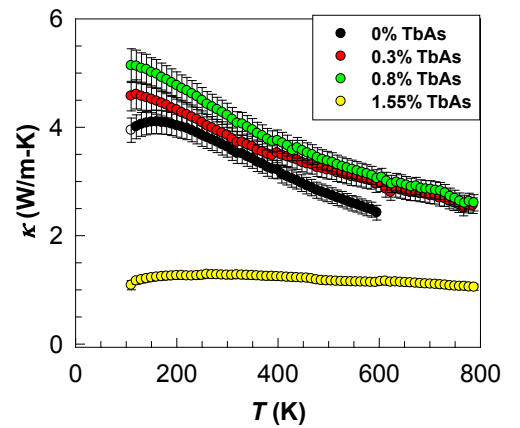


Figure 26 Experimentally measured thermal conductivity of TbAs:InGaAs alloys

thermal conductivity from these samples shows a trend that is opposed to what we expected: material with a higher nanoparticle concentration would have lower thermal conductivity because of mid to long-wavelength phonon scattering in addition to the alloy scattering. We plan to do a detailed comparison of 3 ω measurement results with TDTR to see if we could identify the reason for abnormal thermal conductivity of TbAs:InGaAs samples.

C. Thermal characterization of HfN:ScN superlattices:

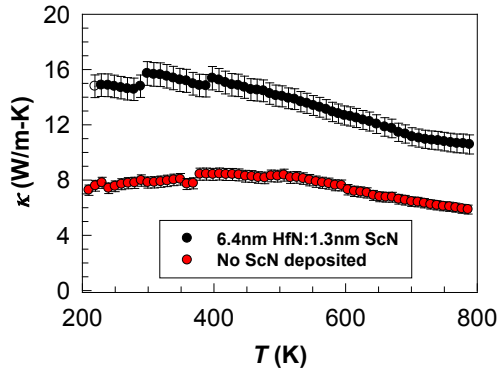


Figure 27 Experimentally measured thermal conductivity of HfN:ScN superlattices grown on silicon substrates

HfN:ScN is a promising material for thermal to electric energy conversion due to its almost perfect lattice match, energy-dependent electron filtering and thermal conductivity reduction across the interfaces. We previously reported the thermal conductivity of (Hf,Zr)N:(Sc,Y)N superlattices. A major issue of the previous nitride samples was possible contamination of Sc. In the past year, we have measured newly grown HfN:ScN superlattices free of W contamination. Figure 27 shows the measured thermal conductivity of the superlattice on a silicon substrate. The bulk-like behavior of thermal conductivity might be due to an imperfect formation of a lattice structure during growth process.

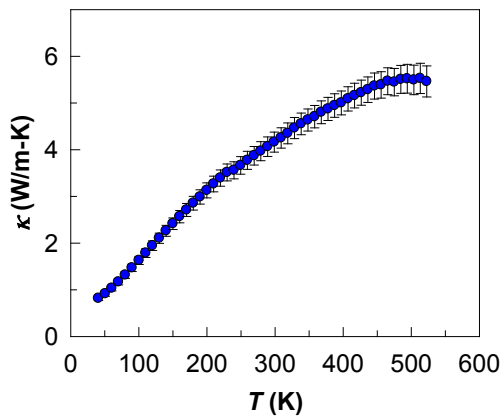


Figure 28 Experimentally measured thermal conductivity of 8.9 nm HfN: 2.6 nm ScN superlattice grown on a MgO substrate

Figure 28 shows the thermal conductivity of the superlattice, grown on an MgO substrate in which lattice spacings are 8.9 nm and 2.6 nm for HfN and ScN, respectively. Above 600K, low thermal conductivity contrast between the sample and background made it difficult to utilize a 3 ω differential method. As shown in Figure 20, phonon contribution in thermal conductivity seems to be less significant as indicated by gradually increasing the thermal conductivity with increasing temperature.

11. Thermoelectric characterizations at MIT

A. Z-meter

The experimental setup (Fig. 29) build at MIT includes a Z-meter with a high temperature ceramic heater, a measure bar and an active load setup for simultaneous measurements of thermoelectric parameters (Seebeck coefficient, electrical conductivity and thermal conductivity), generated power and efficiency.

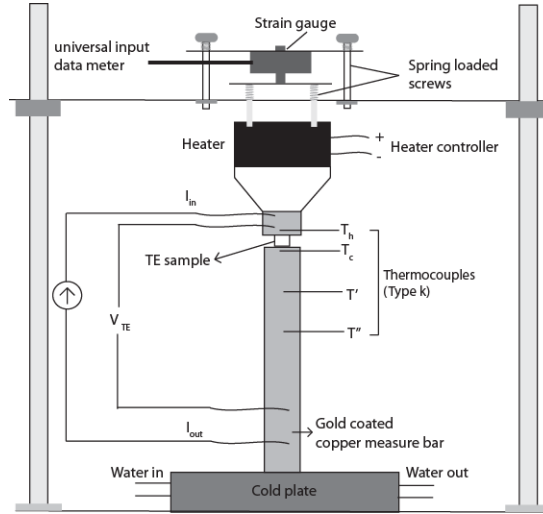


Fig. 29: Z-meter setup for high temperature characterization

Metal/semiconductor superlattice (SL) structures were characterized using the Z-meter. These samples were bulk-laminate structures with stacks of 5 μm SL layers. Initial measurements resulted in very low Seebeck coefficients ($\sim 10\text{s } \mu\text{V/K}$ - similar to metal), primarily due to metal shorts created during dicing process (Fig. 30a). New samples were polished with 3 μm diamond lapping disc to get rid of gold on the edges (Fig. 30b). During initial measurements, it was also noticed that the material degraded considerably at large temperature gradient, primarily due to thermal stress at the contact layers. In order to keep the thermal gradient below 200 K, the Z-meter setup was slightly modified by wrapping a rope heater around the measure bar sitting below the sample.

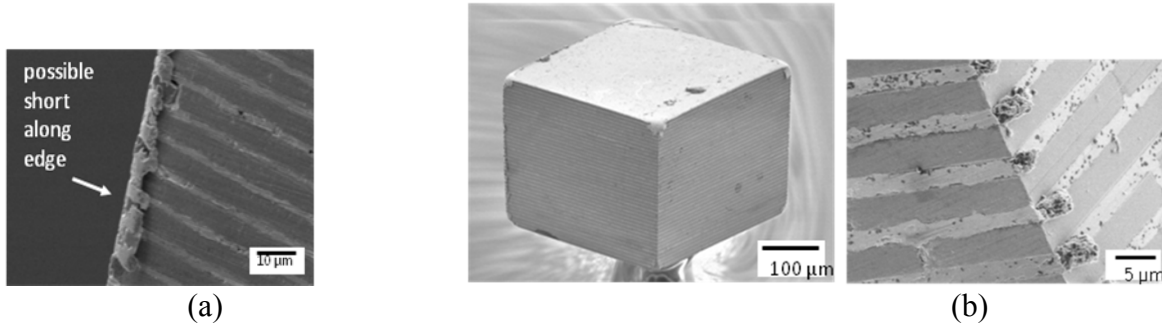


Fig. 30: (a) Nitride superlattice bulk-laminate samples (gold shorts at the edges created during dicing); (b) polished nitride sample with visibly less gold shortenings between TE layers

The first Seebeck coefficient measurement results for (Hf, Zr)N/ScN sample are shown below (Fig. 31a). The sample was 280 μm thick with 40 SL layers (5 μm each) and 80 gold layers (1 μm each). The cross section area was $\sim 300 \mu\text{m} \times 300 \mu\text{m}$. Steady increase in the Seebeck coefficient was measured compared to the previous unpolished samples. The highest Seebeck coefficient $\sim 130 \mu\text{V/K}$ was measured at an average temperature of 830 K, which is comparable to high temperature conventional TE material such as silicon germanium.

The electrical conductivity measurement was dominated by the interface parasitic (Fig. 31b). The matched load resistance showed no dependency on temperature. The estimated Ohmic contact of $1.3 \times 10^{-5} \Omega \text{cm}^2$ is enough to give a resistance of 1.15Ω for 80 gold layered TE sample, indicating that the contact resistance dominates the measurement.

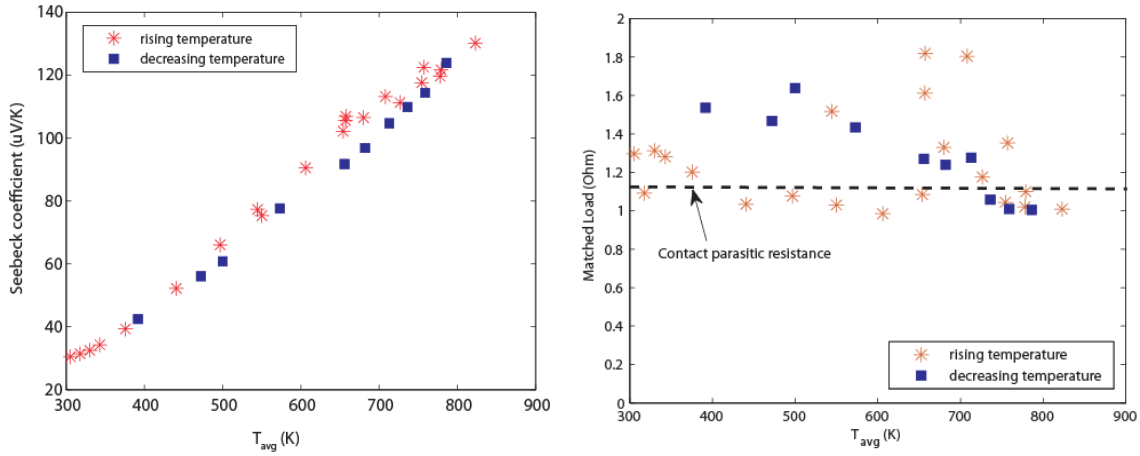


Fig. 31: (a) Seebeck coefficient measured for the nitride SL structure; (b) measured matched load resistance at various average temperatures

The second set of samples measured was CuBond36 (HfN/ScN) metal/semiconductor superlattice structure (Figs. 32-33). These samples had $85 \mu\text{m}$ of active TE superlattices (17 layers - each $5 \mu\text{m}$ thick). The total gold contact layer was $34 \mu\text{m}$. The sample was $110 \mu\text{m} \times 300 \mu\text{m} \times 377 \mu\text{m}$.

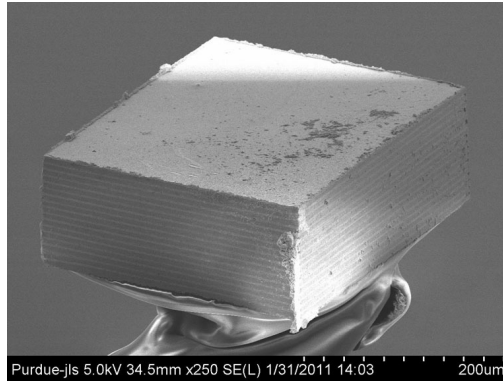


Fig. 32: HfN/ScN superlattice structure ($110 \mu\text{m}$ thick sample)

The thermal conductivity measured between 300-650 K were $2.4\text{-}4.4 \text{ W/m K}$, consistent with $3\text{-}\omega$ measurement for similar samples. The Seebeck coefficient was $20\text{-}65 \mu\text{V/K}$, similar to the previously measured values for the polished sample within the measured temperature range.

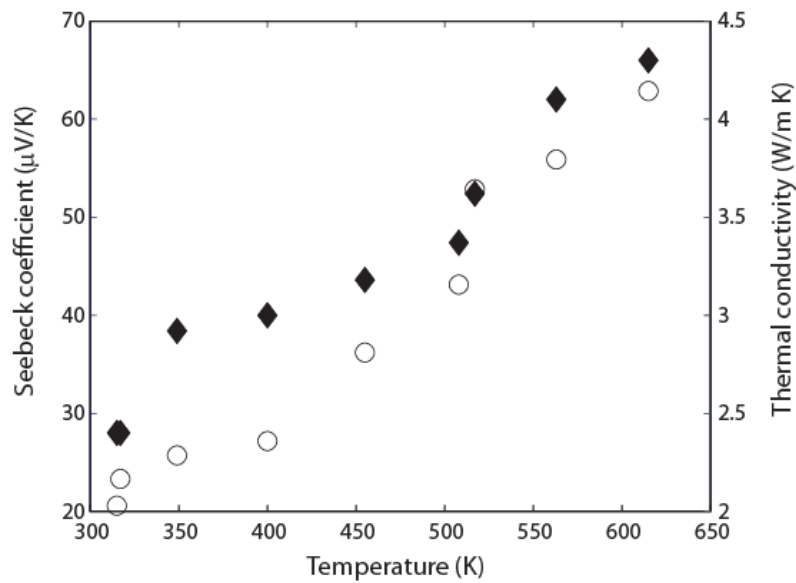


Fig. 33: Measured Seebeck coefficient (○) and thermal conductivity (◆) for CuBond36 sample

The electrical conductivity measurement was again dominated by the interface resistance between gold and the nitride layer. Resistivity of $5\text{e-}6 \Omega\text{cm}^2$ was estimated from Z-meter measurements of electrical resistance. This interface resistivity was 50% lower than the resistivity compared to previous samples. The decrease in parasitic was due to in-situ copper deposition on metallic nitride before depositing Cr/Au contacts. Similar interface resistivity was measured independently at Purdue University.

	Theory (@ 300 K)	1 st Z-meter measurement (@ 340 K) Jan, 2010	2 nd Z-meter measurement (@ 380 K) Feb, 2010	3 rd Z-meter measurement (@ 305 K) Sept, 2010 – Dec, 2010	4 th Z-meter measurement (@ room temp.) March, 2011-May, 2011
Composition	HfN (8nm) / ScN(4nm)	(Hf0.5,Zr0.5)N (6nm)/ScN(6nm)	(Hf0.5,Zr0.5)N (6nm)/ScN(6nm)	(Hf,Zr)N /ScN	(Hf,Zr)N /ScN
Seebeck Coefficient (μV/K)	360 (ZT @ 300K = 0.7)	2.25 (dominated by metallic short)	19	30 (130 @ 825 K)	21 (65 @ 625 K)
Thermal conductivity (W/m K)	2.8	2.7	4.6	2.35	2.4
Electrical conductivity (1/ Ω cm)	500 (6 nm HfN / 6 nm ScN) @ ΔEc = 1040 meV	135	50	Interface parasitic: $1.3\text{e-}5 \Omega\text{cm}^2$	Interface parasitic: $5\text{e-}6 \Omega\text{cm}^2$ (in-situ copper deposition on top of metallic nitride)

B. Sub-micron Mapping Thermal Conductivity of Thermoelectric Thin Films

We have developed micro-instrumentation utilizing the thermoreflectance (TR) technique to characterize thermal conductivity and material uniformity. The instrument, shown in Fig. 26, consists of a heating element for creating temperature gradients; an invar bar with *in situ* temperature monitoring is used for heat flux measurements. The thin-film sample is sandwiched between the heater and invar bar while a microscope is used to direct light onto a cross section of the sample and reflected light is collected with a camera. The changes in reflectivity (ΔR) caused by changes in surface temperature (ΔT), as described by the relationship: $\Delta T = \Delta R / \kappa R$, where κ is the material and wavelength dependent TR coefficient and R is reflectivity at room temperature. By using this technique, we can achieve a high spatial resolution for thermal conductivity and eliminate contributions from thermal contact resistance, but also eliminate the need for sample preparation other than cleaving.

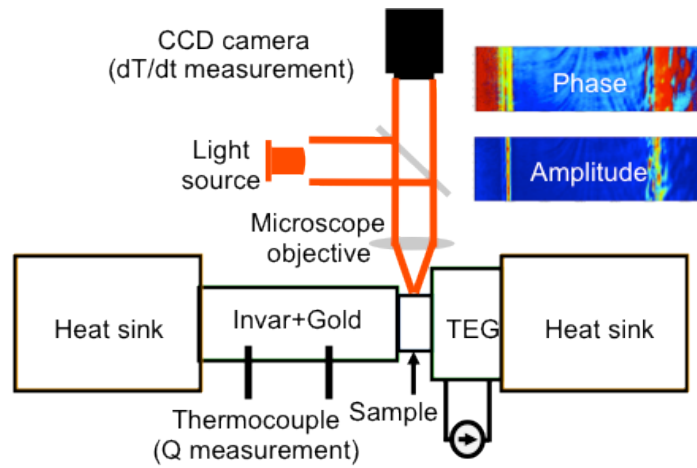


Fig. 34: Schematic diagram of micro-instrumentation for thermal conductivity measurements and mapping.

The instrument is utilized to examine 1) thermal conductivity of a 60 μm ErAs: InGaAlAs TE element and 2) temperature profile across a 5 μm ErAs: InGaAlAs TE element on 45 μm InP substrate. ErAs: InGaAlAs is chosen due to its tendency to cleave along definite smooth planar surfaces determined by its crystal structure, which is crucial for TR measurements. The 60 μm sample has a uniform material composition and is used to validate the accuracy of the measurement.

The sample is cleaved with a smooth surface. It is then cleaned and mounted between the invar bar and the heating element. A 50 mHz sinusoidal current (3A, peak-to-peak) is injected into the TE heater, and phase locked to the camera using two coupled function generators. The images are then taken using trigger frequencies of 200 mHz. For each measurement, 20000 iterations of averaging are performed. The temperature profiles across the sample are shown in Fig. 35. The images are averaged in the transverse direction in order to improve the temperature resolution and obtain a thermal profile of the element along the direction of heat flux. The linear temperature profile indicates that the thermal conductivity remains constant across the sample during the long (24 hours) MBE growth of the sample. It shows the thermal conductivity has less than 7% of variations across the sample.

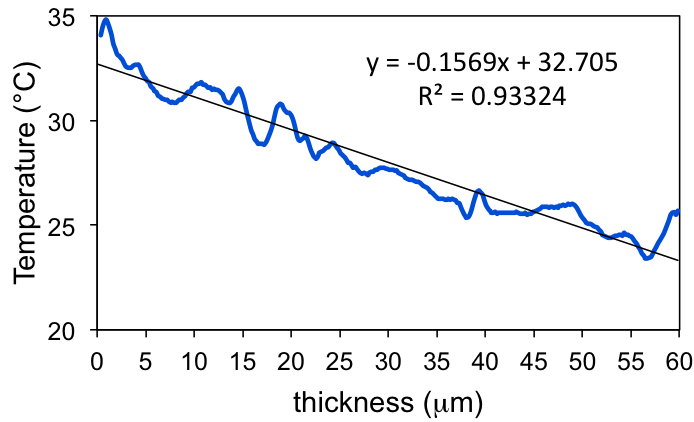


Fig. 35: Temperature profile of the ErAs: InGaAlAs TE element at the modulation frequency of 50 mHz.

To further improve the measurement accuracy, different temperature gradients are created and therefore different heat fluxes are measured across the sample. A linear curve fitting of temperature gradient versus heat flux is shown in Fig. 36. The thermal conductivity of 2.3 W/mK is extracted. The average thermal conductivity obtained with the 3-omega method is 2.5 W/mK.

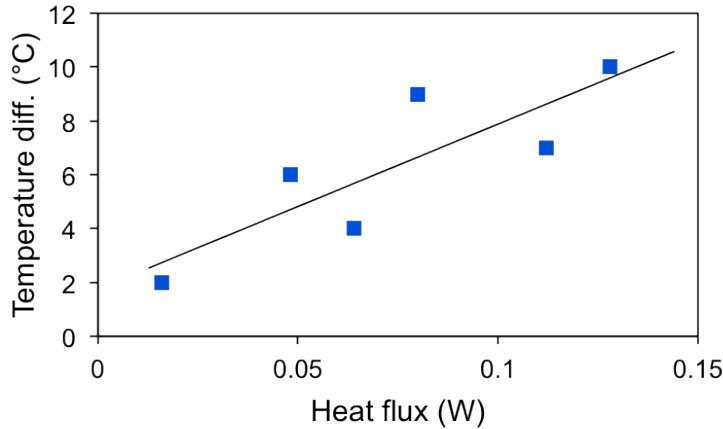


Fig. 36: Temperature difference across ErAs: InGaAlAs TE element as a function of heat flux

The instrument is utilized to examine thermal conductivity variations across a sample consisted of 5 μm of 0.6% ErAs: N-type InGaAlAs on 45 μm of InP substrate. A 100 mHz sinusoidal current (3A, peak-to-peak) is injected into the TE heater, and phase locked to the camera using two coupled function generators. The images are then taken using trigger frequencies of 400 mHz. The temperature profile across the sample is shown in Fig. 37. Two temperature slopes have been observed. This indicates two different thermal conductivities. Most of temperature drop is across the ErAs: N-type InGaAlAs TE element, which shows it has lower thermal conductivity than the InP substrate (68 W/mk).

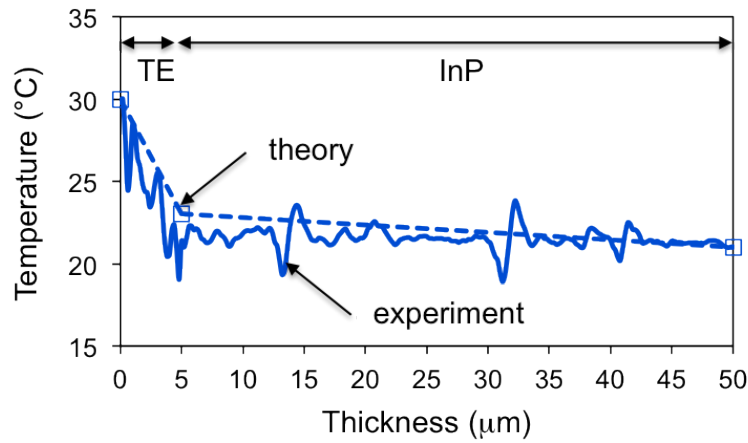


Fig. 37: Temperature profiles of ErAs: InGaAlAs on InP substrate.

12. Nanoscale modeling of charge transport (UCSC, UCSB, MIT)

During the period Aug. 2010 to Jul. 2011, the Bowers group developed a rigorous procedure for calculating transport coefficients of p-type materials including the effects of inelastic and inter-band scattering in a coupled-band model, under the framework of the Boltzmann transport theory. This helped develop appropriate controls for assessing ErSb:InGaSb and other nanocomposites of p-type III-V compound semiconductors and their alloys.

UCSC group calculated the thermoelectric properties of of TbAs:InGaAs samples. The calculations were based on Boltzmann transport equation using relaxation time approximation and included all major electron scattering mechanisms. It turns out that both the ionized impurity scattering and ionized nanoparticle scattering models fit with UCSC's data points quite well, as seen in Fig. 38. UCSB group's measurements gave a little higher Seebeck coefficient. We are currently checking the measurement more carefully to see where the discrepancy comes from.

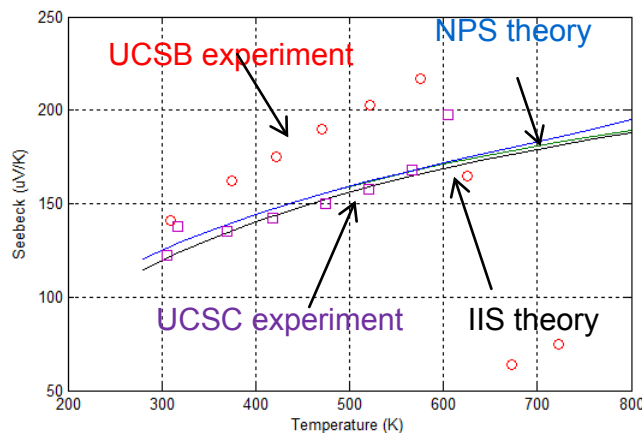


Fig. 38: Measurements and modeling of Seebeck coefficient of TbAs: InGaAs with 0.78% Tb

UCSC group also work with MIT group to study the effects of resonance states of core/shell nanoparticles on thermoelectric transport. Using the partial wave method, we could calculate the electron scattering time of these nanoparticle inclusions, as shown in Fig. 39. The inset is a schematic of the potential of a core/shell nanoparticle. At electron resonance levels, electron has peaks of electron scattering rate. The position, width, and amplitude of these peaks can be tuned by the size, potential steps, barrier width, and effective masses of the core/shell structure. By using the optimal choices of nanoparticles, it is predicted by calculation that a 155% thermoelectric power factor enhancement can be achieved for PbTe at 80K, as shown in Fig. 40. We also performed the same calculation for InGaAs alloys. It turns out that ionized impurity scattering has a major impact and II-VI material (such as PbTe) could benefit more from the core/shell resonant scatters.

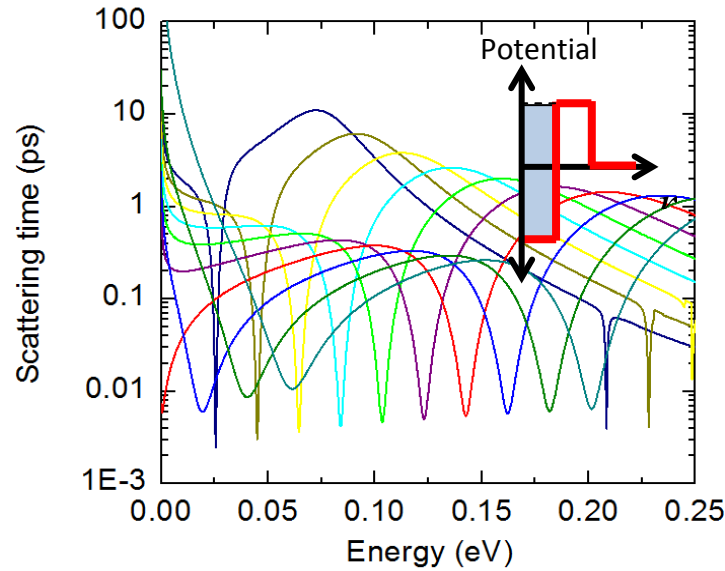


Fig. 39. The electron scattering time of core/shell nanoparticles.

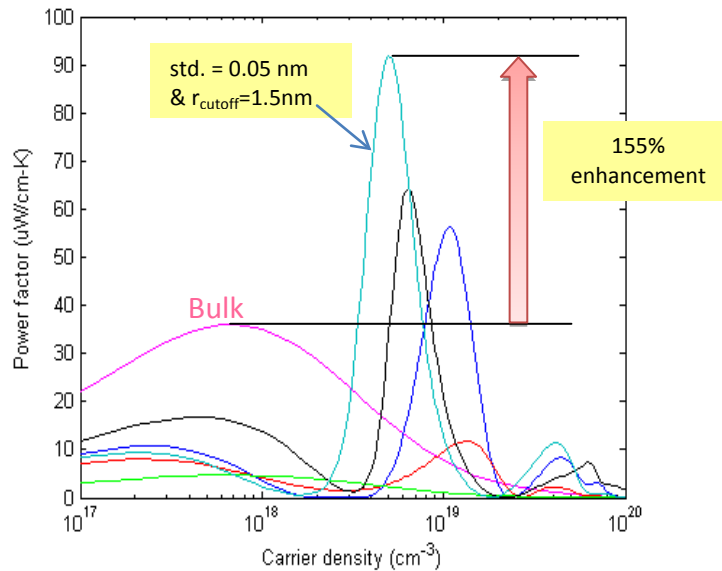


Fig. 40. Thermoelectric power factor for PbTe embedded with core/shell nanoparticles of different size distribution.

13. Predicted Thermal Stress in a Thermoelectric Module (TEM) Design

A simple, easy-to-use and physically meaningful analytical (mathematical) model is developed for the prediction of the interfacial shearing thermal stress in an assembly comprised of two identical components (adherends) subjected, however, to different temperatures. The inhomogeneous bonding system is comprised of a plurality of identical column-like supports located at equal distances (spaces) from each other. One encounters such a situation in a thermoelectric module (TEM) design, where bonding is provided by multiple thermoelectric material (such as, e.g., Bismuth-Telluride-Alloy, Si, or SiGe) supports (legs). The objective of the analysis is to demonstrate that appreciable stress relief could be achieved when the fractional area coverage of TE legs and the spacing between them are optimized. It is imperative, of course, that if thin legs are employed for lower stresses, there is still enough interfacial “real estate”, so that the adhesive strength of the assembly is not compromised. On the other hand, owing to a lower stress level in an assembly with thin legs and large spacing, assurance of its interfacial strength is less of a challenge than for a conventional assembly with stiff, thick and closely positioned legs. Future work will include experimental evaluations of the stress-at-failure for the TEM designs of interest.

Case study

Table I
Mechanical properties of materials employed in TE module

Material	Young Modulus (GPa)	CTE (ppm/ °C)	Poisson's ratio
Ceramic Component	380	6.5	0.28
Copper Stripe (metallization)	115	17	0.31
Sn-Sb solder layer	44.5	27	0.33
Be ₂ Te ₃ leg	47	16.8	0.4

The analytical solution is applied to the TE module structure. The material properties are given in Table I. Three different assembly sizes of 10, 20, and 40 mm ($L=5, 10$, and 20 mm) were chosen. The value of l , the half-length of the bonded regions, has been varied to evaluate its effect on the maximum interfacial shear stress. The temperature difference between the top and the bottom components (ΔT) is 130°C ($160-30$). The thickness of the thermoelectric leg is chosen to be 4 mm. Bonded region and component thicknesses are set according to Fig. 33. The maximum interfacial shear stress versus bonded region length for different assembly lengths is obtained using the analytical model (see Fig. 42). As can be seen, as the bonded region length decreases the maximum interfacial shear stress is reduced. Also, for the same bonded region length increasing the assembly length will decrease the maximum shear stress. This means that by increasing the $L/2l$ ratio, or decreasing the fractional area coverage of the thermoelectric legs the maximum shear stress will drop.

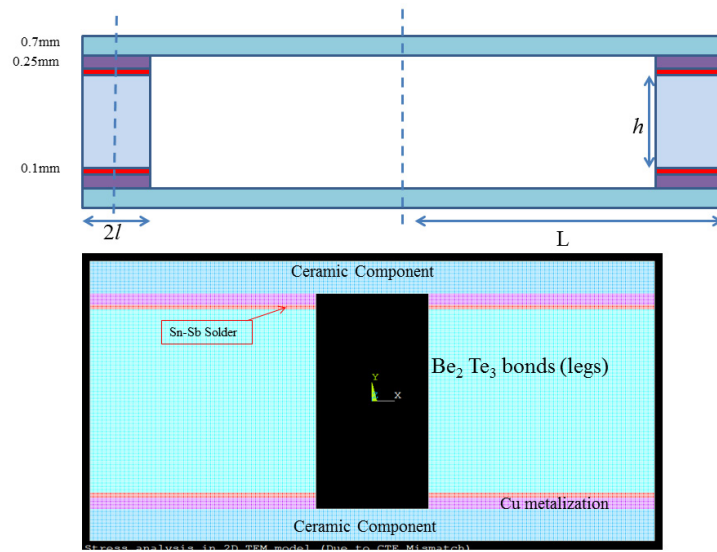


Fig. 41. Dimensions, materials, meshing of a 2D TEM with $L=3.3l$.

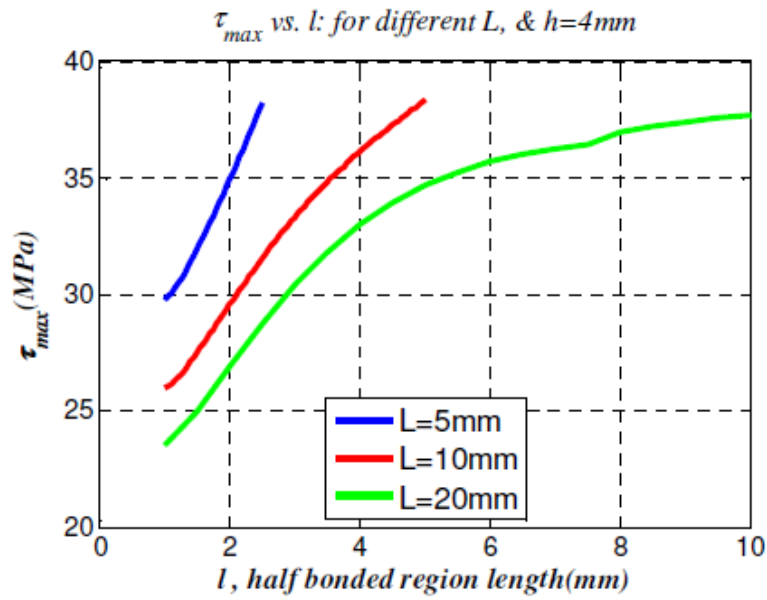


Fig. 42. Variation of maximum interfacial shear stress (τ_{max}) vs. bonded region's length for different assembly lengths, $2L=10$ mm (blue), 20 mm (red), and 40 mm (green).

14. System integration and test (BSST)

During the third year of the project, BSST continued to test bulk materials and they became available and reported the characterizations to the team. BSST also continued work on advanced instrumentation developed to assist in the material testing. Lastly, as part of BSST's Phase II SOW, BSST assessed the manufacturability and scalability of material systems for various thermoelectric applications.

Objective 1: Characterization of new materials.

During this period, BSST received four samples of Gallium Indium Arsenide from Purdue. BSST completed a contour plot (Figure 43) of each sample and created a histogram, demonstrating the quality of homogeneity of each sample. None of the samples tested were found to have promising uniform characteristics. This was one of the main reasons the bulk growth activity using Bridgmann technique was stopped.

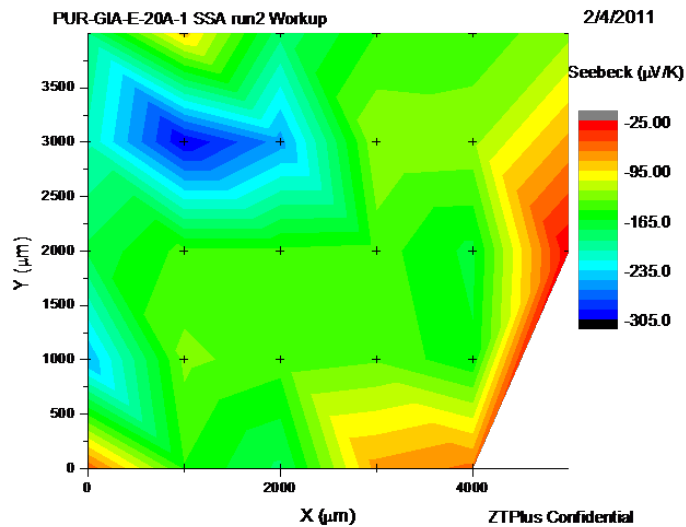


Figure 43. Contour Plot of Purdue Sample PUR-GIA-E-20A-1.

Objective 2: Improve test methodology by developing more advanced test devices and processes.

BSST has designed and built a multi-probe scanning Seebeck tool under this project (Figure 44), allowing for faster and more consistent testing. It will also be useful in analyzing causes of nonuniformity in samples. The tool has been operated in manual mode for initial testing. An x-y stage was acquired and is being placed into the unit. Programming and automation are the next steps for finalizing the tool.

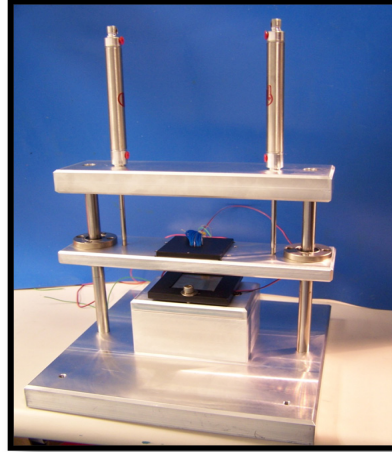


Figure 44. Photograph of Scanning Seebeck tool in frame.

Objective 3: Assess manufacturability of thermoelectric material systems.

Traditional commercial TE materials are generally fabricated from bulk TE materials, with dimensions of 0.5 to 10 mm in the direction of current flow. However, some of the most promising ZT thermoelectric materials have been produced at least initially as films. Two factors reduce device level performance and hence present commercialization challenges for the film TE materials. Both are roughly inversely proportional to the TE material thickness in the direction of current flow:

1. Reduction in device level ZT due to parasitic losses.
2. Increase in internal shear stresses and TE material degradation associated with internal temperature gradients.

Several device geometries are under development to address the limitations imposed by film TE materials. Applications for film materials can be sensors, self powered controls and possibly some spot cooling of electronics. There remains the need to develop bulk versions of promising TE materials especially for potential usage in high volume industrial, residential and vehicle markets for heating, ventilation and air conditioning (HVAC) and waste heat recovery.

One potential direction where thinner TE elements could be useful in big scale energy and power generation applications, is the use of low fractional area coverage thermoelectric elements in a module (Fig. 45). The idea is to use heat concentration through thermoelectric plates and minimize the use of expensive TE material (~\$500/kg for BiTe or PbTe). With 5-10% area coverage, the optimum leg length would be on the order of 0.3-0.5mm. Assuming hot side temperature of 600K, cold reservoir at 300K, Heat flux: $5\sim 7 \times 10^5 \text{ W/m}^2$, element density: $100/\text{cm}^2$, it becomes possible to reduce the cost of material in TE heat recovery system from \$1-2/W to \$0.05-0.1/W with the use of new module geometry with low fractional area coverage.

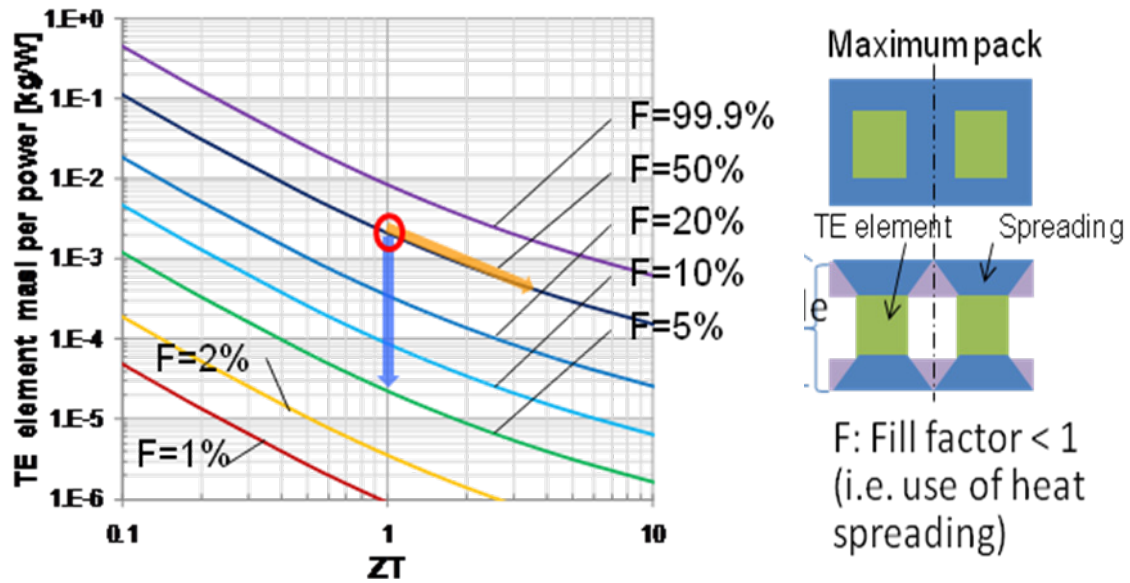


Fig. 45 TE element mass (required for thermal impedance matching) as a function of ZT (reduction in thermal conductivity) and F (fractional area coverage of elements). The idea of heat concentration (low fractional area coverage is shown in the inset).

Manuscripts submitted, but not published (total 1)

Amirkoushyar Ziabari, E. Suhir, A. Shakouri, “Minimizing Thermally Induced Interfacial Shearing Stress in a Thermoelectric Module with Low Fractional Area Coverage,” under review in *Microelectronics Journal*, November 2013.

Papers published in peer-reviewed journals (29)

- 1) A.T. Ramu, L. E. Cassels, N. H. Hackman, H. Lu, J. M. O. Zide, J. E. Bowers, “Rigorous calculation of the Seebeck coefficient and mobility of thermoelectric materials,” *Journal of Applied Physics*, 107, 083707 (2010). <http://dx.doi.org/10.1063/1.3366712>
- 2) J.-H. Bahk, Z. X. Bian, M. Zebarjadi, J. M. O. Zide, H. Lu, D. Xu, J. P. Feser, G. Zeng, A. Majumdar, A. C. Gossard, A. Shakouri, J. E. Bowers, “Thermoelectric Figure of Merit of InGaAlAs III-V semiconductor alloys,” *Physical Review B*, 81, 235209 (2010).<http://dx.doi.org/10.1103/PhysRevB.81.235209>
- 3) J. M. O. Zide, J.-H. Bahk, R. Singh, M. Zebarjadi, G. Zeng, H. Lu, J. P. Feser, D. Xu, S. L. Singer, Z.X. Bian, A. Majumdar, J. E. Bowers, A. Shakouri, and A. C. Gossard, “High efficiency semimetal/semiconductor nanocomposite thermoelectric materials.” *Journal of Applied Physics*, 108, 123702. (2010).<http://dx.doi.org/10.1063/1.3514145>
- 4) Ali Shakouri, Arun Majumdar, Mercouri G. Kanatzidis, Christopher J. Vineis. Nanostructured Thermoelectrics: Big Efficiency Gains from Small Features, *Advanced Materials*, (09 2010): 3970. doi: 10.1002/adma.201000839
- 5) J. M. O. Zide, J.-H. Bahk, R. Singh, M. Zebarjadi, G. Zeng, H. Lu, J. P. Feser, D. Xu, S. L. Singer, Z. X. Bian, A. Majumdar, J. E. Bowers, A. Shakouri, A. C. Gossard. High efficiency semimetal/semiconductor nanocomposite thermoelectric materials, *Journal of Applied Physics*, (12 2010): 123702. doi: 10.1063/1.3514145
- 6) Mona Zebarjadi, Keivan Esfarjani, Zhixi Bian, Ali Shakouri. Low-Temperature Thermoelectric Power Factor Enhancement by Controlling Nanoparticle Size Distribution, *Nano Letters*, (01 2011): 225. doi: 10.1021/nl103581z
- 7) A. T. Ramu, L. E. Cassels, N. H. Hackman, H. Lu, J. M. O. Zide, J. E. Bowers, “Thermoelectric transport in the Coupled Valence-Band Model,” *Journal of Applied Physics*, 109, 033704. (2011). <http://dx.doi.org/10.1063/1.3537826>
- 8) L. E. Cassels, T. E. Buehl, P. G. Burke, C. J. Palmstrøm, A. C. Gossard, G. Pernot, A. Shakouri, C. R. Haughn, M. F. Doty, and J. M. O. Zide, “Growth and characterization of TbAs:GaAs nanocomposites,” *Journal of Vacuum Science and Technology B*, 29, 03C114 (2011).<http://dx.doi.org/10.1116/1.3555388>

- 9) Gilles Pernot, Ali Shakouri, Chelsea R. Haughn, Matthew F. Doty, Joshua M. O. Zide, Trevor E. Buehl, Peter G. Burke, Chris J. Palmstrom, Art C. Gossard, Laura E. Cassels. Growth and characterization of TbAs:GaAs nanocomposites, *Journal of Vacuum Science & Technology B: Microelectronics and Nanometer Structures*, (02 2011): 1071. doi: 10.1116/1.3555388
- 10) Peter G. Burke, Hong Lu, Nicholas G. Rudawski, Susanne Stemmer, Arthur C. Gossard, Je-Hyeong Bahk, John E. Bowers. Electrical properties of Er-doped $\text{In}_{0.53}\text{Ga}_{0.47}\text{As}$, *Journal of Vacuum Science & Technology B: Microelectronics and Nanometer Structures*, (05 2011): 1071. doi: 10.1116/1.3559480
- 11) Hong Lu, Peter G. Burke, Arthur C. Gossard, Gehong Zeng, Ashok T. Ramu, Je-Hyeong Bahk, John E. Bowers. Semimetal/Semiconductor Nanocomposites for Thermoelectrics, *Advanced Materials*, (05 2011): 2377. doi: 10.1002/adma.201100449
- 12) P. G. Burke, T. E. Buehl, P. Gilles, H. Lu, A. Shakouri, C. J. Palmström, J. E. Bowers, and A. C. Gossard, "Controlling n-type carrier density from Er-doping of InGaAs with MBE growth temperature," *J. Electron. Mater.*, vol. 41, no. 5, p. 948, 2012.
- 13) P. G. Burke, T. E. Buehl, G. Pernot, H. Lu, A. Shakouri, C. J. Palmstrom, J. E. Bowers, and A. C. Gossard, "Erratum to: Controlling n-Type Carrier Density from Er Doping of InGaAs with MBE Growth Temperature," *Journal of Electronic Materials*, vol. 41, no. 5, p. 948, Apr. 2012.
- 14) Ali Shakouri. Recent Developments in Semiconductor Thermoelectric Physics and Materials, *Annual Review of Materials Research*, (08 2011): 399. doi: 10.1146/annurev-matsci-062910-100445
- 15) Je-Hyeong Bahk, Zhixi Bian, Mona Zebarjadi, Parthiban Santhanam, Rajeev Ram, Ali Shakouri. Thermoelectric power factor enhancement by ionized nanoparticle scattering, *Applied Physics Letters*, (08 2011): 72118. doi: 10.1063/1.3625950
- 16) R. B. Sadeghian, J.-H. Bahk, Z. Bian, and A. Shakouri, "Calculation of nonlinear thermoelectric coefficients of $\text{InAs}_{1-x}\text{Sb}_x$ using Monte Carlo Method," *J. Electron. Mater.* 41, 1370 (2012). DOI: 10.1007/s11664-011-1858-8
- 17) J.-H. Bahk, P. Santhanam, Z. Bian, R. Ram, and A. Shakouri, "Resonant carrier scattering by core-shell nanoparticles for thermoelectric power factor enhancement," *Appl. Phys. Lett.* 100, 012102 (2012). <http://dx.doi.org/10.1063/1.3673615>
- 18) J.-H. Bahk, R. B. Sadeghian, Z. Bian, and A. Shakouri, "Seebeck enhancement through mini-band conduction in III-V semiconductor superlattices at low temperatures," *J. Electron. Mater.* 41, 1498 (2012). DOI: 10.1007/s11664-012-1917-9
- 19) Hsinyi Lo, Rajeev J. Ram. Sub-micron Mapping Thermal Conductivity of Thermoelectric Thin Films, *Journal of Electronic Materials* 41, 1332 (2012). DOI: 10.1007/s11664-011-

- 20) A. T. Ramu, L. E. Clinger, P. B. Dongmo, J. T. Imamura, J. M. O. Zide, and J. E. Bowers. "Incompatibility of standard III-V compound semiconductor processing techniques with terbium doped InGaAs of high terbium concentration," *Journal of Vacuum Science and Technology A*, 30, 031508 (2012) <http://dx.doi.org/10.1116/1.3701951>.
- 21) E. Selezneva, L. Cassels, A. Ramu, G. Pernot, T. Buehl, T. Favaloro, J. Bahk, Z. Bian, J. Bowers, J. Zide, and A. Shakouri. "Thermoelectric transport in InGaAs with high concentration of rare-earth TbAs embedded nanoparticles." *Journal of Electronic Materials*, 41, 1820. (2012). <http://dx.doi.org/10.1007/s11664-012-2097-3>.
- 22) P. Jha, T. D. Sands, L. Cassels, P. Jackson, T. Favaloro, B. Kirk, J. M. O. Zide, X. Xu, and A. Shakouri, "Cross-plane electronic and thermal transport properties of p-type $\text{La}_{0.67}\text{Sr}_{0.33}\text{MnO}_3/\text{LaMnO}_3$ perovskite oxide metal/semiconductor superlattices." *Journal of Applied Physics*, 112, 064714 (2012). <http://dx.doi.org/10.1063/1.4754514>
- 23) L. E. Clinger, G. Pernot, T. E. Buehl, A. C. Gossard, C. J. Palmström, A. Shakouri, and J. M. O. Zide, "Thermoelectric properties of epitaxial TbAs:InGaAs nanocomposites." *Journal of Applied Physics*, 111, 094312 (2012). <http://dx.doi.org/10.1063/1.4711095>
- 24) E. Suhir, A. Shakouri, "Assembly Bonded at the Ends: Could Thinner and Longer Legs Result in a Lower Thermal Stress in a Thermoelectric Module Design?" *Journal of Applied Mechanics*, Vol. 79, pp. 0610101-0610108, Nov. 2012. (DOI: 10.1115/1.4006597)
- 25) Kazuaki Yazawa and Ali Shakouri, "Scalable Cost/Performance Analysis for Thermoelectric Waste Heat Recovery Systems," *Journal of Electronic Materials*, vol. 41, No. 6, Apr. 2012. (DOI: 10.1007/s11664-012-2049-y)
- 26) E. Suhir, A. Shakouri, "Predicted thermal stress in a multileg thermoelectric module (TEM) design," *Journal of Applied Mechanics*, vol. 80, 021012, Mar. 2013. (DOI: 10.1115/1.4007524)
- 27) Polina V. Burmistrova, Jesse Maassen, Tela Favaloro, Bivas Saha, Shuaib Salamat, Yee Rui Koh, Mark S. Lundstrom, Ali Shakouri, and Timothy D. Sands, "Thermoelectric properties of epitaxial ScN films deposited by reactive magnetron sputtering onto $\text{MgO}(001)$ substrates," *Journal of Applied Physics* 113, 153704, Apr. 2013. (DOI: 10.1063/1.4801886)
- 28) Pankaj Jha, Timothy D. Sands, Philip Jackson, Cory Bomberger, Tela Favaloro, Stephen Hodson, Joshua Zide, Xianfan Xu, and Ali Shakouri, "Cross-plane thermoelectric transport in p-type $\text{La}_{0.67}\text{Sr}_{0.33}\text{MnO}_3/\text{LaMnO}_3$ oxide metal/semiconductor superlattices," *Journal of Applied Physics* 113, 193702, May 2013. (DOI: 10.1063/1.4804937)
- 29) Schroeder, J.L.; Ewoldt, D.A.; Amatya, R.; Ram, R.J.; Shakouri, A.; Sands, T.D., "Bulk-Like Laminated Nitride Metal/Semiconductor Superlattices for Thermoelectric Devices," *Microelectromechanical Systems*, *Journal of*, no.99, pp.1, October 2013; doi:

Presentations at conferences/ Invited presentations (45)

1. Ali Shakouri, Invited talk “Design of High Performance, Robust and Low Cost Thermoelectric Modules,” MRS Fall Meeting, Symposium B, Boston, MA; November 2012
2. Ali Shakouri, Invited talk “Nanoscale Electrothermal Energy Transport,” Cornell University; November 2012
3. Ali Shakouri, Invited talk “Cost Efficiency Trade Off in Nanostructured Thermoelectric Systems,” American Vacuum Society 59th Annual International Symposium, Tampa, Florida; 29 October 2012
4. Ali Shakouri, Invited Talk, “Nanostructured thermoelectric energy conversion and refrigeration devices,” Device Research Conference, Penn State University; June 2012
5. Ali Shakouri, Invited Talk, “Nanostructured materials for thermoelectric conversion,” SPIE (International Society for Optics and Photonics) Defense, Security + Sensing, Baltimore, MD; April 2012
6. Ali Shakouri, Invited Talk, “Nanostructured thermoelectric materials for waste heat recovery,” Symposium on Nanomaterials for Energy, Purdue University; April 2012
7. Ali Shakouri, Invited Talk, “Linear and Non-linear Thermoelectric Transport for Waste Heat Recovery,” BNNI (Berkeley Nanosciences and Nanoengineering Institute) Seminar, Berkeley, CA; February 2012
8. Ali Shakouri, Invited Talk, “Symposium W: Phonons in Nanomaterials-Theory, Experiments, and Applications,” 2011 MRS (Materials Research Society) Fall Meeting Symposium, Boston, MA; November 2011
9. Ali Shakouri, Invited Talk, “Nanostructured thermoelectric materials for waste head recovery applications and for microfrigeration,” Princeton University, November 2011
10. (invited) “Semimetal/semiconductor nanostructured composites for thermoelectric applications”, Hong Lu, University of Texas, Austin, Texas, June 2011.
11. (invited) “Semimetal/semiconductor nanostructured composites for thermoelectrics” Hong Lu, University of Notre Dame, Indiana, March 2011.
12. (invited) A. Shakouri, “Material tradeoffs in direct thermal to electric energy conversion systems,” American Physical Society March Meeting, Symposium on Materials for Energy, Dallas, TX, March 2011

13. J. M. O. Zide, "Enhancing Efficiency in Thermoelectrics with MBE-grown Tb(Er)As/InGaAs Nanocomposites," Presented at North American Conference on MBE, San Diego, CA, 2011.
14. J. M. O. Zide, "Novel Semiconductors and Epitaxial Nanocomposites for Applications in Thermoelectrics, Terahertz, and Optoelectronics" Presented at National Institute of Standards and Technology, Boulder, CO, 2011.
15. J. M. O. Zide, "Novel Semiconductor and Epitaxial Nanocomposite Materials for Energy Conversion Applications" Presented at Millersville University, Millersville, PA (2011).
16. R. Amatya and R.J. Ram, "Trend for thermoelectric materials and their earth abundance," International Thermoelectrics Conference, 2011.
17. Laura E. Cassels, Ashok T. Ramu, Gilles Pernot, Trevor E. Buehl, Peter G. Burke, Art C. Gossard, Chris J. Palmstrøm, Ali Shakouri, John E. Bowers,, "Improving Thermoelectric Power Generation Efficiency with Epitaxial TbAs/III-V Nanocomposites." the 2011 Electronic Materials Conference, Santa Barbara, CA (2011).
18. Hong Lu, Peter Burke, Nathan H. Hackman, John E. Bowers, Arthur C. Gossard, "Thermoelectric properties of ErSb:In_xGa_{1-x}Sb thin films grown by MBE", Electronic Materials Conference 2011, Santa Barbara, CA, June 22-24, 2011
19. P. G. Burke, J. E. Bowers, and A. C. Gossard, "Nanoparticle size dependence of the electrical, thermal, and optical properties of Er-doped In_{0.53}Ga_{0.47}As," Electronic Materials Conference 2011, Santa Barbara, CA, June 22-24, 2011
20. Zhixi Bian, Je-Hyeong Bahk, Mona Zebarjadi, Ali Shakouri, Parthiban Santhanam and Rajeev J. Ram "Effects of Nanoparticle Resonant States on Thermoelectric Transport," Materials Research Symposium, April 2011
21. Burmistrova, P., Schroeder, J., Wortman, R., Jackson, P., Shakouri, A., & Sands, T. (2011). Microstructure and Thermoelectric Properties of Nitride Metal/Semiconductor Superlattices for High-Temperature Energy Conversion. 30th International Conference on Thermoelectrics (ICT 2011).
22. T. Onishi, K. J. Norris, E. Colman, V. Wong, A. Shakouri, G. S. Tompa, N. P. Kobayashi, "MOCVD growth of erbium monoantimonide thin films and nanocomposites for thermoelectrics", ICT 2011.
23. Laura E. Cassels, Gilles Pernot, Trevor E. Buehl, Art C. Gossard, Chris J. Palmstrøm, Ali Shakouri, Joshua M. O. Zide, "Improving Thermoelectric Power Generation Efficiency with epitaxial TbAs/III-V Nanocomposites." ICT 2011.
24. L. Cassels, P. Dongmo, A. Ramu, G. Pernot, T. Buehl, A. Gossard, A. Shakouri, C. Palmstrøm, J. Bowers, J. M. O. Zide, "Enhancing Efficiency in Thermoelectrics with MBE-

grown Tb(Er)As/InGaAs Nanocomposites,” North American Conference on Molecular Beam Epitaxy, San Diego, CA (2011).

25. Schroeder JL, Ewoldt D, Burmistrova P, Wortman R, and Sands TD, “Laminated Nanostructured Metal/Semiconductor Superlattices for Bulk-like Thermionic Energy Conversion Devices,” AMN-5 (Advanced Materials and Nanotechnology Conference), Wellington, New Zealand, February 11th, (2011).
26. J. M. O. Zide, Optical, electrical, and thermal properties of TbAs:(In)GaAs Nanocomposites, Workshop on embedded nanoparticles, Santa Barbara, CA (2011).
27. AMN-5 2011 (Advanced Materials and Nanotechnology Conference), Laminated Nanostructured Metal/Semiconductor Superlattices for Bulk-like Thermionic Energy Conversion Devices, Presenter: Jeremy L. Schroeder
28. A. Shakouri, Invited Talk, “Transient charge and energy transport in thermoelectric devices,” Workshop on New Trends in Nonlinear Dynamics: Heat Control and Thermoelectricity (HEAT 2010), Erice, Italy; October 2010
29. A. Shakouri, Invited Talk, “Thermoelectric transport in nanostructured materials,” Workshop on Electronic Transport in Nanoengineered Materials, University of Chicago, IL; September 2010
30. Hong Lu, Peter Burke, Gehong Zeng, John Bowers, Arthur C. Gossard, “MBE grown ErSb:InxGa1-xSb and its application in thermoelectrics”, 27th North American Molecular Beam Epitaxy Conference, Breckenridge, CO, September 27, 2010
31. P. G. Burke, H. Lu, N. G. Rudawski, S. Stemmer, J.-H. Bahk, T. Favaloro, A. Shakouri, J. E. Bowers, and A. C. Gossard, "Electrical and optical properties of nanoparticle thermoelectric power generation materials," 27th North American Molecular Beam Epitaxy Conference, Breckenridge, CO, September 27, 2010
32. J. M. O. Zide, “Improved Thermoelectric Performance in Epitaxial Metal/Semiconductor Nanocomposites,” Army Workshop on Advanced Concepts in Semiconductor Materials and Devices for Energy Conversion, Beltsville, MD (2010).
33. J. M. O. Zide, “Improved Thermoelectric Performance in Epitaxial Metal/Semiconductor Nanocomposites,” Advanced Concepts in Semiconductor Materials and Devices for Energy Conversion, Beltsville, MD (2010).
34. P.V. Burmistrova, J.L. Schroeder, D.A. Ewoldt, R. Amatya, R. Ram, and T.D. Sands, “Nitride Metal/Semiconductor Superlattices for High-Temperature Solid-State Energy Conversion,” 2010 MRS Spring Meeting, San Francisco, CA, April 8th (2010).
35. R. Wortman, J. Schroeder, P. Burmistrova, L. Cassels, T. Sands, and J. Zide, “Epitaxial Growth of Transition Metal Nitrides on MgO via DC Magnetron Sputtering,” Electronic

Materials Conference, June 25th (2010).

36. Schroeder JL, Ewoldt D, Burmistrova P, Wortman R, and Sands TD, “Bulk-like Thermionic Energy Conversion Device Fabricated from Laminated Nanostructured Metal/Semiconductor Superlattices,” 2010 Electronic Materials Conference, University of Notre Dame, June 25th (2010).
37. Schroeder JL, Ewoldt D, Burmistrova P, Wortman R, and Sands TD, “Bridging the gap between nano and micro for advanced thermoelectric materials/devices,” UGIM 2010 (University Government Industry Micro/Nano Symposium), Purdue University, July 1st (2010).
38. J. M. O. Zide. “Novel Metal/Semiconductor Nanocomposite and Superlattice Materials and Devices for Thermoelectrics” SPIE – Defense, Security, and Sensing. Orlando, FL (2010).
39. J. M. O. Zide, A. Shakouri, and A. Majumdar. “The Use of Nanoparticle Inclusions to Reduce Thermal Conductivity in Thermoelectrics.” Advances in Peltier Cooling Workshop, Air Force Research Laboratory, Albuquerque, NM (2009).
40. J. M. O. Zide. “Metal/Semiconductor Nanocomposites and Electron Filtering Effects for Thermoelectric Applications.” 8th Pacific Rim Conference on Ceramic and Glass Technology. Vancouver, BC, Canada. (2009).
41. P.V. Burmistrova, J.L. Schroeder, R. Wortman, and T.D. Sands, “Microstructure and Thermoelectric Properties of HfN/ScN Metal/Semiconductor Superlattices for Thermionic Energy Conversion,” Poster N3.9, 2009 MRS Spring Meeting, San Francisco, CA (2009).
42. J. Schroeder, P. Burmistrova, R. Wortman and T.D. Sands, “Alternative Substrates for Metal/Semiconductor Superlattices for Thermionic Energy Conversion,” L8, 2009 Electronic Materials Conference, Penn. St. University (2009).
43. J. Schroeder, P. Burmistrova, R. Wortman, D. Ewoldt and T. Sands, “Metal/Semiconductor Superlattices on Silicon Substrates for Solid-State Thermionic Energy Conversion Devices,” Z 2.7, 2009 MRS Fall Meeting, Boston, MA, November 30th (2009).
44. R. Wortman, J. Schroeder, P. Burmistrova, T. Sands, M. Zebarjadi, Z. Bian, and A. Shakouri, “Nitride Metal-Semiconductor Superlattices for Solid-State Thermionic Energy Conversion”, American Physics Society March Meeting, Pittsburgh, PA, March (2009).
45. R. Wortman, J. Schroeder, P. Burmistrova, T. Sands, M. Zebarjadi, Z. Bian, and A. Shakouri, “Solid State Thermionic Direct Thermal to Electrical Energy Conversion with Nitride Metal-Semiconductor Superlattices,” International Conference on Thermoelectrics, Freiburg, Germany, July (2009).

Honors and Awards

(1) Joshua M. O. Zide: 2011 North American Molecular Beam Epitaxy Young Investigator

Number of Patents Disclosed: 1**List of patent titles disclosed**

(1) "EFFECTIVE AND SCALABLE SOLAR ENERGY COLLECTION AND STORAGE,"
Kazuaki YAZAWA, Zhixi BIAN, Ali SHAKOURI

Number of Patents Awarded: 2**List of patent titles awarded:**

(1) United States Patent Application, EFS ID 8939363, LAMINATED THIN FILM METAL-SEMICONDUCTOR MULTILAYERS FOR THERMOELECTRICS, (Jeremy L. Schroeder and Timothy D. Sands)

(2) Provisional United States Patent, EFS ID- 9611658, P-TYPE LANTHANUM STRONTIUM MANGANATE/LANTHANUM MANGANATE PEROVSKITE OXIDE METAL/SEMICONDUCTOR SUPERLATTICES FOR THERMOELECTRICS, (Pankaj Jha and Timothy D. Sands)

Technology Transfer (any specific interactions or developments which would constitute technology transfer of the research results). Examples include interaction with other DOD scientists, interactions with industry, initiation of a start-up company based on research results or transfer of information which might impact the development of products.

(1) Structured Materials Industries, Inc. (Piscataway, New Jersey) has obtained several SBIRs from DOE and from NASA in order to commercialize their antimonide MOCVD reactor. Structured Material Industries, Inc. grew all of the rare-earth InGaSb and InAsSb material in the phase I of the DARPA project as they were optimizing Prof. Nobby Kobayashi's reactor to be installed at UC Santa Cruz. The work on Prof. Kobayashi's system allowed SMI to develop a new MOCVD system which has applications beyond thermoelectrics in high speed electronics and in infrared imaging.

(2) The DARPA funding has enabled BSST to invest in improving test devices and methodology which speeds characterization of materials that BSST is preparing to commercialize. As a part of this research, BSST has developed an experimental multi-probe scanning Seebeck tool. The advances of this tool allow for: (a) significantly improving the time to collect data - minutes rather than days; (b) a more thorough analysis of uniformity; and (c) diagnosing conditions that are the cause of non-uniformities.

(3) With technical assistance from U. C. Berkeley, UCSB group implemented the "Three-Omega" method for measuring thermal conductivity of thin films and substrates. Funding under DARPA for

the implementation of the Three-Omega method in UCSB had a positive impact on other thermoelectrics and photonics efforts in UCSB, as evidenced by the fact that the hardware, data acquisition software and numerical analysis software⁴ developed under this project is routinely utilized by other research groups.

(4) InP-based materials were specifically chosen due to the maturity of both the materials and the processing technologies associated with them. In this portion of the project, Delaware group is maintaining close communications with other project members to ensure smooth technology transfer is possible. More specifically, we are remaining in close contact with the Bowers group about the integration of these materials into new devices and on processing techniques, discussing how we can provide guidelines for more-readily-commercialized bulk materials with team members at Purdue, and especially remaining in close discussions with BSST about requirements for project materials for eventual technology transfer into devices and systems which will meet the needs of Department of Defense (and other) customers. Based on these discussions, we are focusing heavily on InGaAs-based materials.